JACS
JOURNAL OF THE AMERICAN CHEMICAL SOCIETY
Article
pubs.acs.org/JACS

Role of the Metal in the Bonding and Properties of Bimetallic Complexes Involving Manganese, Iron, and Cobalt

Stephen J. Tereniak,[†] Rebecca K. Carlson,[†,‡] Laura J. Clouston,[†] Victor G. Young, Jr.,[†] Eckhard Bill,*[,§] Rémi Maurice,[†,‡] Yu-Sheng Chen,[∥] Hyun Jung Kim,[†,‡] Laura Gagliardi,*[,†,‡] and Connie C. Lu*[,†]

[†]Department of Chemistry, University of Minnesota, 207 Pleasant Street SE, Minneapolis, Minnesota 55455-0431, United States
[‡]Supercomputing Institute and Chemical Theory Center, University of Minnesota, Minneapolis, Minnesota 55455, United States
[§]Max Planck Institut für Chemische Energiekonversion, Stiftstraße 34-36, 45470 Mülheim an der Ruhr, Germany
[∥]ChemMatCARS, University of Chicago, Argonne, Illinois 60439, United States

Supporting Information

ABSTRACT: A multidentate ligand platform is introduced that enables the isolation of both homo- and heterobimetallic complexes of divalent first-row transition metal ions such as Mn(II), Fe(II), and Co(II). By means of a two-step metalation strategy, five bimetallic coordination complexes were synthesized with the general formula $M_1M_2Cl(py_3tren)$, where py_3tren is the triply deprotonated form of *N*,*N*,*N*-tris(2-(2-pyridylamino)ethyl)amine. The metal−metal pairings include dicobalt (**1**), cobalt−iron (**2**), cobalt−manganese (**3**), diiron (**4**), and iron−manganese (**5**). The bimetallic complexes have been investigated by X-ray diffraction and X-ray anomalous scattering studies, cyclic voltammetry, magnetometry, Mössbauer spectroscopy, UV−vis−NIR spectroscopy, NMR spectroscopy, combustion analyses, inductively coupled plasma optical emission spectrometry, and ab initio quantum chemical methods. Only the diiron chloride complex in this series contains a metal−metal single bond (2.29 Å). The others show weak metal−metal interactions (2.49 to 2.53 Å). The diiron complex is also distinct with a septet ground state, while the other bimetallic species have much lower spin states from $S = 0$ to $S = 1$. We propose that the diiron system has delocalized metal−metal bonding electrons, which seems to correlate with a short metal−metal bond and a higher spin state. Multiconfigurational wave function calculations revealed that, indeed, the metal−metal bonding orbitals in the diiron complex are much more delocalized than those of the dicobalt analogue.

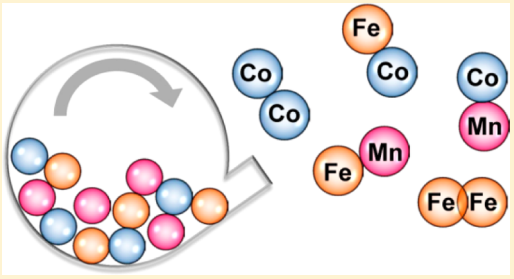

INTRODUCTION

Heterometallic clusters are used as bioinorganic cofactors to perform diverse chemical reactions. They occur in MoFe and VFe nitrogenases, [NiFe] hydrogenases, purple acid phosphatases, Ni-[3Fe-4S] CO dehydrogenases, and class Ic ribonucleotide reductases (RNRs).[1−4] Many of these heterometallic cofactors pair a mid- and late-first-row transition metal (e.g., Fe and Ni) to promote the heterolytic activation of small molecules, (e.g., H_2 and CO_2).[5] In contrast, class Ic RNRs use two *similar* metals, Fe and Mn, to tune the redox properties of the cofactor.[6,7] The heterometallic cofactor is unique to this subclass, as most class I RNRs use a classical diiron(II,II) active site with a neighboring tyrosine.[8] When the diiron cofactor reacts with dioxygen, a diiron(III,III)−tyrosyl radical [i.e., 2Fe(III)−Y·] intermediate is formed, where the reactive hole equivalent is located on the amino acid. It has been proposed that since class Ic RNRs lack this tyrosine, an iron site is swapped for manganese to store the oxidizing equivalent as the Fe(III)−Mn(IV) intermediate.[9−13] To better understand the different roles of iron versus manganese, Fe−Mn complexes have been targeted, but only a few biomimetic Fe−Mn complexes have been reported.[14−17] A key challenge is the selective preparation and/or clean isolation of the heterometallic core when the metal centers are so similar.[16]

Beyond their bioinorganic relevance, heterometallic clusters may give rise to unusual magnetic and electronic properties. Indeed, Fe−Mn complexes have been studied to elucidate magnetic exchange interactions.[18−21] Betley and co-workers have shown that the homotrimetallic clusters Fe_3, Co_3, and Mn_3 exhibit interesting magnetic behavior and are extending their studies to mixed-metal analogues.[22−25] Also, as in the case of class Ic RNRs, swapping of metal sites with similar transition metals could prove to be a versatile strategy for tuning redox potentials. In related work, Agapie and co-workers have shown that the redox potentials of Mn_3−oxide clusters can be systematically tuned by ∼700 mV by covalently attaching redox-inactive metal centers of varying Lewis acidity.[26,27] Systematic studies of heterobimetallic species may provide great insight into structure−property relationships and hold promise for achieving predictable and precise control of cluster properties through metal atom substitution.

Received: September 6, 2013
Published: October 14, 2013

   dx.doi.org/10.1021/ja409016w | *J. Am. Chem. Soc.* 2014, 136, 1842−1855

Of note, nearly all these examples contain a bridging oxo, phenoxo, or amido ligand, which can greatly attenuate the metal−metal interaction. We have been interested in configuring bonds between first-row transition metals by using ligands that facilitate metal−metal bonding.[28−30] Recently, the use of multidentate ligands with two distinct binding sites enabled the synthesis of a rare iron−cobalt heterobimetallic complex.[31] The same ligand also gave access to a related dicobalt complex. Both the iron−cobalt and dicobalt species have short metal−metal bonds and are high-spin. However, attempts to extend the coordination chemistry to other similar metal pairings were unsuccessful.

Herein we report a new ligand variant wherein three pyridyl groups are covalently attached to tris(2-aminoethyl)amine (tren). The ligand, *N,N,N*-tris(2-(2-pyridylamino)ethyl)amine, or $H_3(py_3tren)$, has enabled the isolation of homo- and heterobimetallic complexes of cobalt, iron, and manganese. Five bimetallic chloride complexes, $M_1M_2Cl(py_3tren)$ (see Key),

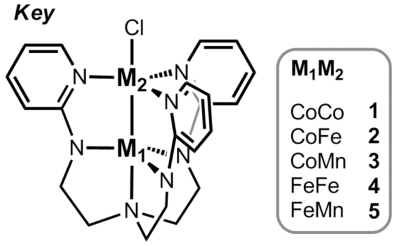

have been isolated and characterized by a host of physical methods. Since standard X-ray diffraction experiments do not differentiate between similar transition metals, the heterobimetallic species were further examined by both X-ray anomalous scattering and inductively coupled plasma optical emission spectrometry (ICP-OES) for analysis of single crystals and the bulk material, respectively. Two of the three heterobimetallic complexes (CoMn **3** and FeMn **5**) showed only a slight degree of metal-site mixing, while CoFe **2** was contaminated by CoCo **1** (8%). The good to high purity of these heterobimetallic complexes is remarkable given the propensity of high-spin Co(II), Fe(II), and Mn(II) ions to undergo ligand exchange and thus effect metal scrambling.

This isostructural bimetallic family presents a unique opportunity to systematically study the effect of the metal identity on the metal−metal bonding as well as on their electronic and magnetic properties.[30,32−35] We have found that the metal−metal interactions are generally weak, with the notable exception of diiron chloride **4**, which contains a bona fide iron−iron bond. With the exception of **4**, the electrochemical and magnetic properties of the bimetallic family can be rationalized by considering these bimetallic species as individual metals or as localized spins that couple antiferromagnetically, giving lower spin states. In contrast, complex **4**, which has an $S = 3$ ground state, does not fit the localized description. Theoretical studies revealed delocalized metal−metal bonding in **4**, which is correlated with its different magnetic behavior. Finally, the isotropic magnetic couplings for the bimetallic complexes were computed using density functional theory (DFT) with various exchange−correlation functionals.

EXPERIMENTAL SECTION

General Considerations. Unless otherwise stated, manipulations were performed under a dinitrogen atmosphere inside a glovebox. Standard solvents were deoxygenated by sparging with N_2 and dried by passing them through activated alumina columns of an SG Water solvent purification system. Benzylpotassium (KBn) was prepared according to literature methods.[36] Deuterated solvents were purchased from Cambridge Isotope Laboratories, degassed via freeze−pump−thaw cycles, dried over activated alumina, and stored over activated 4 Å molecular sieves. Tris(2-aminoethyl)amine (tren) was purchased from Pressure Chemical Co. All other reagents were purchased from Aldrich or Strem and used without further purification. Elemental analyses were performed by Complete Analysis Laboratories (Parsippany, NJ). ICP-OES data were collected at the University of Minnesota Earth Sciences Analytical Geochemistry Lab using a Thermo Scientific iCAP 6500 dual-view instrument with the addition of cesium as a matrix modifier and yttrium as an internal standard. The weight percents are averages of three or four measurements and are reported with standard deviations.

Syntheses. *N,N,N-Tris(2-(2-pyridylamino)ethyl)amine ($H_3[py_3tren]$).* Tren (9.77 g, 66.8 mol), 2-bromopyridine (20.0 mL, 210 mmol), and K_2CO_3 (47.0 g, 268 mmol) were heated at 180 °C in 200 mL of DMSO for 3 days. After the crude reaction mixture was cooled to room temperature (rt), it was diluted into $CHCl_3$ and washed with NaOH (1×) and brine (4×). After removal of the volatiles from the organic layer, the crude product was warmed to 50 °C in toluene and loaded onto a silica gel column. The crude product was purified by silica gel chromatography (3:1:0.12 hexanes/EtOAc/7 N NH_3 in CH_3OH). The product fractions were combined, and the solvents were removed in vacuo. The product was dried overnight in vacuo at 60 °C, brought into the glovebox, extracted with THF, and dried in vacuo at 50 °C overnight. This workup provided the product as a tan solid (14.2 g, 56%). ^{1}H NMR (500 MHz, $CDCl_3$): δ 8.05 (dd, $^3J_{HH}$ = 6 Hz, $^4J_{HH}$ = 1 Hz, 1H), 7.31 (ddd, $^3J_{HH}$ = 8 Hz, $^3J_{HH}$ = 6 Hz, $^4J_{HH}$ = 1 Hz, 1H), 6.52 (t, $^3J_{HH}$ = 6 Hz, 1H), 6.32 (d, $^3J_{HH}$ = 8 Hz, 1H), 5.61 (br, 1H, N*H*), 3.30 (app q, $^3J_{HH}$ = 6 Hz, 2H), 2.78 (t, $^3J_{HH}$ = 6 Hz, 2H). ^{13}C NMR (126 MHz, $CDCl_3$): δ 159.0, 148.2, 137.4, 113.0, 108.0, 53.5, 40.0. ESI-MS-TOF *m/z*: $[M + H]^+$ calcd for $C_{21}H_{28}N_7$, 378.2401; found, 378.2426.

K[Co(py$_3$tren)]. To a cold solution of $H_3[py_3tren]$ (0.995 g, 2.64 mmol) in 30 mL of THF, a cold solution of KBn (1.06 g, 8.14 mmol) in 60 mL of THF was added dropwise (CO_2/acetone coldwell bath). After 30 min of stirring, $CoCl_2$ (0.361 g, 2.78 mmol) was added, and then the green solution was immediately removed from the cold bath and stirred overnight. The reaction solution was filtered through Celite and dried in vacuo to give a green resin. The resin was stirred in 3 × 10 mL of Et_2O and 10 mL of pentane and then dried in vacuo for several hours, yielding K[Co(py$_3$tren)] as a fine green powder (1.10 g, 88% yield). ^{1}H NMR (300 MHz, THF-d_8): δ 140, 88, 34, 0.3, −36. UV−vis−NIR (CH_2Cl_2) λ_{max}/nm (ε/L mol^{-1} cm^{-1}): 314 (24 500), 347 sh (10 100), 386 sh (6700), 595 (110), 1620 (80). Anal. Calcd for $C_{21}H_{24}N_7CoK$: C, 53.38; H, 5.12; N, 20.75. Found: C, 53.31; H, 5.19; N, 20.69.

K[Fe(py$_3$tren)]. A solution of $H_3[py_3tren]$ (0.392 g, 1.04 mmol) in 10 mL of THF was deprotonated with a solution of KBn (0.407 g, 3.13 mmol) in 10 mL of THF at rt and stirred for several hours. $FeCl_2$ (0.132 g, 1.04 mmol) was then added, and the reaction mixture was stirred overnight. The mixture was then filtered through Celite and dried in vacuo to yield a red-orange resin. The resin was stirred in 2 × 10 mL of Et_2O and 10 mL of pentane and then dried in vacuo. The resultant powder was then rinsed with 2 × 5 mL of toluene, 1 × 5 mL of Et_2O, and 2 × 5 mL of hexanes and dried in vacuo for several hours, yielding K[Fe(py$_3$tren)] as an orange powder (0.215 g, 44% yield). ^{1}H NMR (300 MHz, THF-d_8): δ 183, 82.4, 30.9, 14.3, −23.6, −33.7. UV−vis−NIR (THF) λ_{max}/nm (ε/L mol^{-1} cm^{-1}): 311 (14 100), 489 (2000), 1650 (40). Anal. Calcd for $C_{21}H_{24}N_7FeK$: C, 53.73; H, 5.15; N, 20.89. Found: C, 53.68; H, 5.08; N, 20.81.

*CoCoCl(py$_3$tren) (**1**).* To K[Co(py$_3$tren)] (639 mg, 1.36 mmol) in 100 mL of THF was added $CoCl_2$ (176 mg, 1.36 mmol) at rt. The green solution rapidly turned into a dark-green suspension. After 11 h of stirring, the volatiles were removed in vacuo. The crude material was then extracted repeatedly with CH_2Cl_2 and filtered through Celite. The filtrate was dried in vacuo, and the resultant residue was dissolved

dx.doi.org/10.1021/ja409016w | J. Am. Chem. Soc. 2014, 136, 1842−1855

Table 1. Crystallographic Details for the $M_1M_2Cl(py_3tren)$ Series, where M_1M_2 = CoCo (1), CoFe (2), CoMn (3), FeFe (4), and FeMn (5)

	1	2	3	4	5
chemical formula	$C_{21}H_{24}N_7Co_2Cl$	$C_{21}H_{24}N_7CoFeCl$	$C_{21}H_{24}N_7CoMnCl$	$C_{21}H_{24}N_7Fe_2Cl$	$C_{21}H_{24}N_7FeMnCl$
formula weight	527.78	524.70	523.79	521.62	520.71
crystal system	orthorhombic	monoclinic	monoclinic	monoclinic	monoclinic
space group	$P2_12_12_1$	$P2_1/n$	$P2_1/n$	$P2_1/n$	$P2_1/n$
a (Å)	9.5866(7)	9.2450(6)	9.3125(7)	9.206(3)	9.3535(4)
b (Å)	14.845(1)	12.5597(8)	12.5159(9)	12.673(3)	12.5109(5)
c (Å)	14.957(1)	18.475(1)	18.574(1)	18.423(5)	18.5566(8)
α (deg)	90	90	90	90	90
β (deg)	90	98.724(1)	98.631(1)	100.544(3)	98.5002(4)
γ (deg)	90	90	90	90	90
V (Å^3)	2128.7(3)	2120.4(2)	2140.4(3)	2113(1)	2147.7(2)
Z	4	4	4	4	4
D_{calcd} (g cm^{-3})	1.647	1.644	1.625	1.640	1.610
λ (Å), μ (mm^{-1})	0.71073, 1.708	0.71073, 1.617	0.71073, 1.514	0.71073, 1.524	0.71073, 1.412
T (K)	123(2)	173(2)	173(2)	173(2)	173(2)
θ range (deg)	1.93 to 27.62	1.97 to 27.42	1.97 to 27.48	1.96 to 27.48	1.97 to 27.48
reflns collected	25021	23646	24156	23676	24203
unique reflns	4782	4801	4900	4831	4918
data/restraints/parameters	4782/0/280	4801/0/281	4900/0/280	4831/0/281	4918/0/280
R_1, wR_2 [$I > 2\sigma(I)$]	0.0186, 0.0477	0.0226, 0.0591	0.0297, 0.0645	0.0234, 0.0660	0.0265, 0.0622

in CH_2Cl_2 and layered with hexanes, yielding 312 mg of a dark-green-brown solid (0.591 mmol, 43% yield). X-ray-quality crystals were grown by layering Et_2O onto a THF solution. ^{1}H NMR (300 MHz, CD_2Cl_2): δ 21.7, 20.9, 11.5, 7.7, 6.7, −1.6. UV−vis−NIR (CH_2Cl_2) λ_{max}/nm (ε/L mol^{-1} cm^{-1}): 317 (28 700), 340 sh (17 900), 450 (8500), 572 (620), 650 (680), 1027 (130), 1650 (40). Anal. Calcd for $C_{21}H_{24}N_7Co_2Cl$: C, 47.79; H, 4.58; N, 18.58. Found: C, 47.77; H, 4.52; N, 18.61.

CoFeCl(py$_3$tren) (2). To a cold THF slurry of $FeCl_2(THF)_{1.5}$ (121 mg, 0.515 mmol), a cold solution of K[Co(py$_3$tren)] (243 mg, 0.514 mmol) was added dropwise (CO_2/acetone coldwell bath). After the mixture was stirred overnight, the volatiles were removed in vacuo. The resultant residue was dissolved in CH_2Cl_2 and filtered through Celite. The filtrate was concentrated in vacuo to 10 mL, filtered again, and layered with Et_2O to obtain 137 mg (0.261 mmol, 51% yield) of dark-red-orange crystals. UV−vis−NIR (CH_2Cl_2) λ_{max}/nm (ε/L mol^{-1} cm^{-1}): 317 (25 000), 356 sh (11 500), 448 (7500), 574 sh (420), 1258 (90). ^{1}H NMR (300 MHz, CD_2Cl_2): δ 32.5, 26.6, 16.8, 1.7, −3.6, −20.3. Anal. Calcd for $C_{21}H_{24}N_7CoFeCl$: C, 48.07; H, 4.61; N, 18.69. Found: C, 48.13; H, 4.56; N, 18.78. ICP-OES (wt %): Fe, 10.96(3); Co, 11.83(2); this is consistent with $Co_{1.01}Fe_{0.99}$.

CoMnCl(py$_3$tren) (3). To a cold THF slurry of $MnCl_2(THF)_2$ (116 mg, 0.431 mmol), a cold solution of K[Co(py$_3$tren)] (203 mg, 0.430 mmol) was added dropwise (CO_2/acetone coldwell bath). The mixture immediately turned green-yellow. After the reaction mixture was stirred overnight, it was dried in vacuo, redissolved in 60 mL of CH_2Cl_2, and filtered through Celite. X-ray-quality crystals were grown from Et_2O layered on a concentrated CH_2Cl_2 solution (141 mg, 0.269 mmol, 63% crystalline yield). ^{1}H NMR (500 MHz, CD_2Cl_2): δ 40, 31.1, 28.6, −9.2, −24.4, −39.4. UV−vis−NIR (CH_2Cl_2) λ_{max}/nm (ε/L mol^{-1} cm^{-1}): 317 (22 600), 349 sh (9800), 397 sh (6800), 435 (9000), 608 (140), 1260 (90). Anal. Calcd for $C_{21}H_{24}N_7CoMnCl$: C, 48.15; H, 4.62; N, 18.72. Found: C, 48.09; H, 4.69; N, 18.71. ICP-OES (wt %): Mn, 12.21(7); Co, 12.81(2); this is consistent with $Co_{0.99}Mn_{1.01}$.

FeFeCl(py$_3$tren) (4). A THF solution of K[Fe(py$_3$tren)] (300 mg, 0.639 mmol) was added to a THF slurry of $FeCl_2(THF)_{1.5}$ (163 mg, 0.690 mmol) at rt. The mixture rapidly turned dark red. After the reaction mixture was stirred overnight and filtered, the filtrate was dried in vacuo, redissolved in 80 mL of CH_2Cl_2, and filtered through Celite. Dark-red crystals were grown from Et_2O layered on a CH_2Cl_2 solution (94 mg, 0.18 mmol, 28% crystalline yield). ^{1}H NMR (500 MHz, CD_2Cl_2): δ 168, 77.5, 42.1, 9.5, 0.8, −15.7. UV−vis−NIR (CH_2Cl_2) λ_{max}/nm (ε/L mol^{-1} cm^{-1}): 310 (18 000), 530 (5600), 997 (190). Anal. Calcd for $C_{21}H_{24}N_7Fe_2Cl$: C, 48.36; H, 4.64; N, 18.80. Found: C, 48.32; H, 4.69; N, 18.73.

FeMnCl(py$_3$tren) (5). To a cold THF slurry of $MnCl_2(THF)_2$ (58 mg, 0.22 mmol), a cold solution of K[Fe(py$_3$tren)] (101 mg, 0.215 mmol) was added dropwise (CO_2/acetone coldwell bath). The mixture immediately turned orange. After the reaction mixture was stirred overnight, it was dried in vacuo, redissolved in 80 mL of CH_2Cl_2, and filtered through Celite. The filtrate was dried in vacuo to give a bright-orange solid. Orange crystals (49 mg, 0.094 mmol, 44% crystalline yield) were obtained from Et_2O layered on a CH_2Cl_2 solution. ^{1}H NMR (500 MHz, CD_2Cl_2): δ 43.7, 16.8, 12.6, 6.5, 2.0, −0.3. UV−vis−NIR (CH_2Cl_2) λ_{max}/nm (ε/L mol^{-1} cm^{-1}): 310 (14 400), 498 (2600), 1019 (40), 1555 (60). Anal. Calcd for $C_{21}H_{24}N_7FeMnCl$: C, 48.44; H, 4.65; N, 18.83. Found: C, 48.33; H, 4.63; N, 18.88. ICP-OES (wt %): Mn, 12.13(2); Fe, 10.6(1); this is consistent with $Fe_{0.92}Mn_{1.08}$.

X-ray Crystallographic Data Collection and Refinement of the Structures. Single crystals of K[Co(py$_3$tren)] were grown from a mixture of pentane, Et_2O, and THF [see Supporting Information (SI) Table 1 for crystallographic data]. Single crystals of CoCoCl(py$_3$tren) (**1**) were grown from Et_2O layered on a THF solution. Single crystals of CoFeCl(py$_3$tren) (**2**), CoMnCl(py$_3$tren) (**3**), FeFeCl(py$_3$tren) (**4**), and FeMnCl(py$_3$tren) (**5**) were grown from Et_2O layered on a CH_2Cl_2 solution. A green plate of K[Co(py$_3$tren)], red blocks of **2** (0.40 mm × 0.20 mm × 0.20 mm) and **4** (0.50 mm × 0.20 mm × 0.20 mm), a green block of **3** (0.60 mm × 0.40 mm × 0.20 mm), and an orange block of **5** (0.40 mm × 0.40 mm × 0.20 mm) were placed on the tip of a glass capillary and mounted on a Bruker APEX II Platform CCD diffractometer for data collection at 173(2) K, and data for a green block of **1** (0.40 mm × 0.40 mm × 0.20 mm) were collected at 123(2) K. The data collection was carried out using Mo Kα radiation (graphite monochromator). The data intensities were corrected for absorption and decay (SADABS). Final cell constants were obtained from least-squares fits of all measured reflections. The structures were solved using SHELXS-97 and refined using SHELXL-97. In each case, a direct-methods solution was calculated that provided most of the non-hydrogen atoms from the E-map. Full-matrix least-squares/difference Fourier cycles were performed to locate the remaining non-hydrogen atoms. All of the non-hydrogen atoms were refined with anisotropic displacement parameters. Hydrogen atoms were placed in ideal positions and refined as riding atoms with relative isotropic

displacement parameters. The crystallographic data for **1**−**5** are summarized in Table 1.

Anomalous Diffraction Data Collection and Refinement of Metal Occupancies. Single crystals of the heterobimetallic compounds **2**, **3**, and **5** were mounted on a glass fiber and cooled to 100 K using an Oxford Instruments Cryojet cryostat. The Bruker D8 diffractometer, integrated with an APEX-II CCD detector, was modified for synchrotron use at the ChemMatCARS 15-ID-B beamline at the Advanced Photon Source (Argonne National Laboratory). For each crystal, diffraction data were collected at seven different energies with 0.3 s frames while manually attenuating the beam to minimize overages of individual pixels. The scan at 30.0 keV (λ = 0.41328 Å), which is energetically far from any atomic absorption energies, gave a least-squares refinement of all model positional and displacement parameters to 0.5 Å resolution. In addition, six anomalous diffraction data sets per complex were collected to span the absorption K edges of both M_1 and M_2 [at the two metals' K edges (λ_{edge}) and ±50 eV]. The following specific energies (keV) [wavelengths (Å)] were used: for iron, 7.062 [1.7557], 7.112 [1.7433], and 7.162 [1.7312]; for cobalt, 7.659 [1.6188], 7.709 [1.6083], and 7.759 [1.5980]; for manganese, 6.489 [1.9107], 6.539 [1.8961], and 6.589 [1.8817]. The anomalous diffraction can distinguish Mn/Fe/Co compositions at the two metal sites because of the expected differences in the anomalous scattering factors ($\Delta f'$ and $\Delta f''$) for these elements, as shown in Figure 1. Basically, the $\Delta f'$ and $\Delta f''$ values of an element change dramatically near the element's absorption edge, while for the other element(s) they remain relatively constant. Each anomalous diffraction data set thus provides a different view of the electrons present at the two sites. Of the six anomalous data sets collected per compound, only two sets ($\lambda > \lambda_{edge}$) were used to solve for the metal occupancies. The others were excluded for the following reasons. For $\lambda = \lambda_{edge}$, the data were less reliable because of inaccuracies in the metal K-edge energies, which shift for coordination compounds. For $\lambda < \lambda_{edge}$, the data were also less reliable because of potential problems with adsorption and/or fluorescence.[37] For each complex, the two anomalous data sets were simultaneously used in a least-squares refinement to determine the Mn/Fe/Co occupancies at the two metal sites (M_1 and M_2). GSAS-II was employed because it allows multiple diffraction data sets as input with subsequent refinement using a common crystallographic model.[38] The 30 keV data were refined using structural models of **2**, **3**, and **5** that had been previously determined at 173 K. The converged positional and displacement parameters were then frozen, so that only the metal occupancies were refined. The crystallographic data are summarized in SI Table 2.

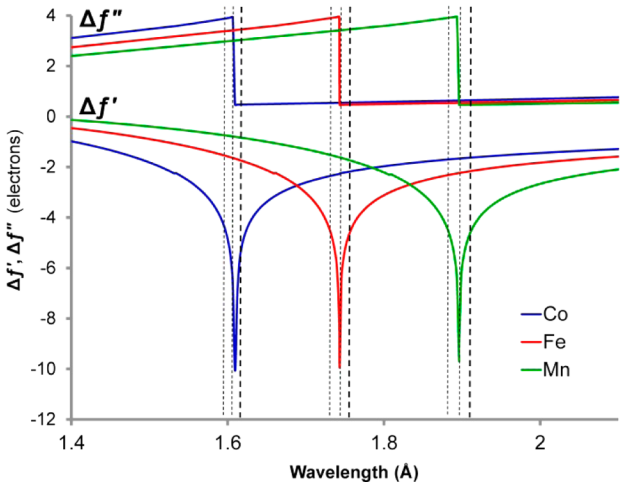

Figure 1. Theoretical anomalous dispersion corrections, including the real ($\Delta f'$) and imaginary ($\Delta f''$) scattering factors, for Co (blue), Fe (red), and Mn (green) as functions of wavelength. The dashed lines represent the experimental wavelengths (λ) for the anomalous data collections, which were selected to span the Co, Fe, and Mn absorption edge energies. The data sets collected at $\lambda > \lambda_{edge}$ (bold dashed lines) were used to determine the metal occupancies.

Physical Measurements. NMR spectra were collected on Varian Inova 300 and 500 MHz spectrometers. UV−vis−NIR absorption data were collected on a Cary-14 spectrophotometer. Cyclic voltammetry was conducted using a CH Instruments 600 electrochemical analyzer. The one-cell setup utilized a platinum working electrode, Pt wire counter electrode, and $Ag/AgNO_3$ reference electrode in CH_3CN. Analyte solutions were prepared in a THF solution of NBu_4PF_6 (0.4 M) and referenced externally to the $FeCp_2/FeCp_2^+$ redox couple. Mössbauer data were recorded on an alternating constant-acceleration spectrometer. The minimum experimental line width was 0.24 mm s^{-1} (full width at half-height). The ^{57}Co/Rh source (1.8 GBq) was positioned at rt inside the gap of the magnet system at a zero-field position. Isomer shifts are quoted relative to iron metal at 300 K.

Magnetic susceptibility data were measured from powder samples of solid material over the temperature range 2−300 K using a SQUID susceptometer with a field of 1.0 T (MPMS-7, Quantum Design, calibrated with a standard palladium reference sample, error <2%). The experimental data were corrected for underlying diamagnetism using tabulated Pascal's constants ($\chi_{dia} < 0$)[39,40] as well as for temperature-independent paramagnetism ($\chi_{TIP} > 0$).[41] Specifically, χ_{TIP} (units of 10^{-6} emu) was 630 for **1**, 860 for **2**, 550 for **4**, and 350 for **5**. Also, in the simulation of **1**, a very small (0.4%) $S = {}^3/_2$ impurity [i.e., monocobalt(II)] was taken into account. The susceptibility and magnetization data were simulated with the program julX for exchange-coupled systems.[42] The simulations were based on the usual spin Hamiltonian operator for mononuclear complexes with spin **S**:

$$\hat{H}_e = g\beta\hat{\mathbf{S}}\cdot\mathbf{B} + D[\hat{S}_z^2 - \frac{1}{3}S(S+1) + \frac{E}{D}(\hat{S}_x^2 - \hat{S}_y^2)]$$

where g is the average electronic g value and D and E/D are the axial zero-field splitting and rhombicity parameters, respectively. After diagonalization of the Hamiltonian, magnetic moments were calculated from the eigenfunctions using the Hellmann−Feynman theorem: $\boldsymbol{\mu}_i(\mathbf{B}) = \langle\psi_i|\partial\hat{H}/\partial\mathbf{B}|\psi_i\rangle$. Intermolecular interactions were considered by using the Weiss temperature, Θ_W, as a perturbation of the temperature scale for the calculation: $k_BT' = k_B(T - \Theta_W)$. Powder summations were performed using a 16-point Lebedev grid. For the bimetallic complexes, we adopted two subspins $\mathbf{S}_1$ and $\mathbf{S}_2$ (one per metal) with an exchange coupling constant J, as defined by:

$$\hat{H} = -2J\hat{\mathbf{S}}_1\cdot\hat{\mathbf{S}}_2 + \hat{H}_{e,1} + \hat{H}_{e,2}$$

Computational Methods. *CASSCF/CASPT2 Calculations.* All of the complete-active-space self-consistent field (CASSCF) calculations, which were followed by perturbation theory to second order (CASPT2), were performed with the MOLCAS 7.8 package[43] on experimental structures without symmetry constraints. Relativistic all-electron ANO-RCC basis sets were used for all elements.[44,45] Double-ζ-quality (ANO-RCC-VDZP) basis sets were used for Co, Fe, Mn, N, and Cl atoms, and minimal basis sets (ANO-RCC-MB) were used for C and H atoms. The following contractions were used: [5s4p2d1f] for the metals, [3s2p1d] for N and Cl, [2s1p] for C, and [1s] for H. To include scalar relativistic effects in the calculation, the Douglas−Kroll−Hess Hamiltonian[46,47] was used. Resolution of identity combined with the Cholesky decomposition (RICD) was used to reduce the computational cost associated with the treatment of two-electron integrals.[48] Lowest-energy solutions were calculated for all spin states at the CASSCF level of theory, and subsequent CASPT2 calculations were performed to recover more dynamical correlation, in which an imaginary level shift of 0.2 au was used to prevent the occurrence of intruder states.[49]

The active spaces for the five complexes were chosen to include the 10 valence 3d electrons plus two correlating 4d orbitals. The active spaces for **1**, **2**, **3**, and **5** respectively, were (14,12), (13,12), (12,12), and (11,12), respectively, where (n_e, n_o) denotes n_e electrons in n_o

dx.doi.org/10.1021/ja409016w | J. Am. Chem. Soc. 2014, 136, 1842−1855

Scheme 1. Two-Step Metalation Reactions: (1) Synthesis of K[Co(py$_3$tren)] and K[Fe(py$_3$tren)]; (2) Synthesis of M$_1$M$_2$Cl(py$_3$tren) Complexes 1−5

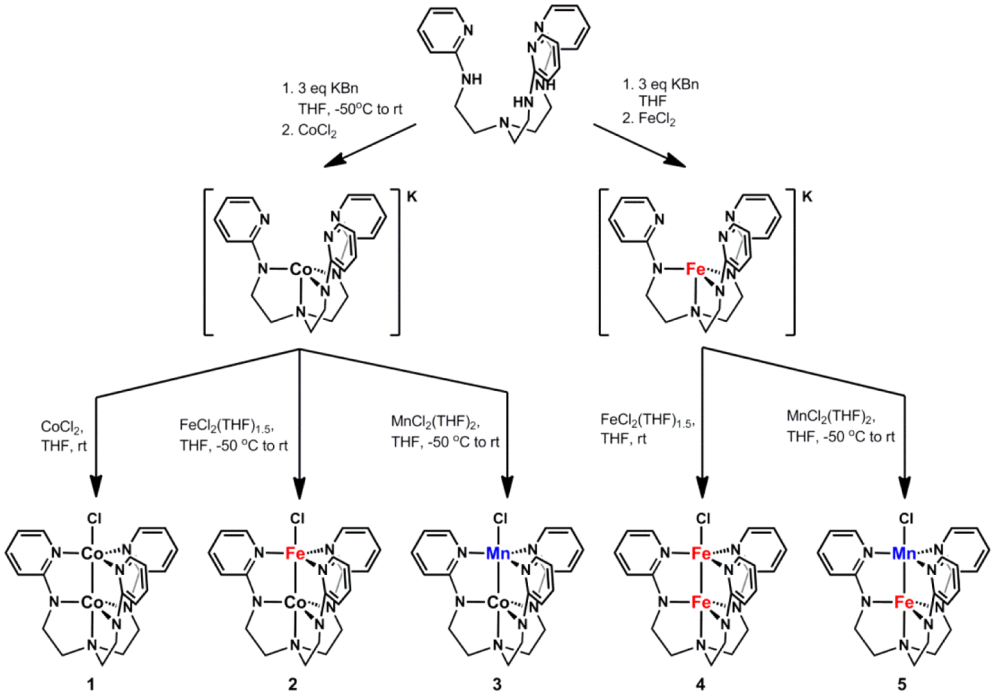

orbitals. Only 12 active orbitals were considered in order to obtain a reasonable level of accuracy while limiting the computational cost. Diiron complex **4** was a more challenging system and required the use of a larger active space. Thus, restricted-active-space (RAS) SCF calculations including a large configuration interaction space were performed, denoted by (12,20)/(12,10)/2. In this notation, the first set of parentheses corresponds to the total number of electrons in RAS1 and RAS2 and the total number of orbitals in all of the RAS spaces, and the second set of parentheses corresponds to the number of active electrons and orbitals in RAS2; the final value of 2 indicates the number of particles allowed into RAS3.

The natural orbital occupation numbers were used for the evaluations of the effective bond order (EBO), which was calculated as the difference between the total occupancies of the bonding and antibonding molecular orbitals of the metal−metal bond divided by 2.[50,51]

DFT Calculations. DFT calculations were performed to evaluate the magnitude of the isotropic magnetic couplings between the two metal centers in **1**, **2**, **3**, and **5**. As proposed by Noodleman for weakly coupled systems, magnetic coupling constants in two-spin systems can be obtained from a high-spin solution and a spin-symmetry-broken solution within spin unrestricted formalisms.[52] The isotropic magnetic couplings were introduced via the phenomenological Heisenberg−Dirac−van Vleck (HDVV) Hamiltonian,

$$\hat{H}^{\mathrm{HDVV}} = -2\sum_{ij} J_{ij}\hat{\mathbf{S}}_i\cdot\hat{\mathbf{S}}_j$$

where $\hat{\mathbf{S}}_i$ and $\hat{\mathbf{S}}_j$ are the spin operators on magnetic centers i and j, respectively, and J_{ij} is the coupling constant between them. The difference between the energies of the spin-symmetry-broken (BS) solution and the high-spin (HS) solution were used to extract the coupling values. In Noodleman's approach, or the weak-coupling limit scheme, the BS solution is considered to be an ideal mixture of spin states corresponding to the appropriate Clebsch−Gordan coefficients. This situation corresponds to the case in which there is no orbital overlap between the magnetic centers i and j. In the studied complexes, a significant overlap between the (local) magnetic orbitals is possible, and thus, we chose to use the intermediate coupling scheme proposed by Yamaguchi:[53]

$$(\langle S^2\rangle^{\mathrm{HS}} - \langle S^2\rangle^{\mathrm{BS}})J_{ij} = E_{\mathrm{BS}} - E_{\mathrm{HS}}$$

where $\langle S^2\rangle^{\mathrm{HS}}$ and $\langle S^2\rangle^{\mathrm{BS}}$ are the expectation values of the total-spin-squared operator coming from the spin-unrestricted calculations. All of the DFT calculations were performed with the Gaussian 09 program package.[54] The BS solutions were obtained from the HS solutions by flipping the spins on one of the magnetic centers and breaking all of the symmetry and spin constraints up to a stable solution using the *stable=opt* keyword of Gaussian 09. Three functionals, a global hybrid functional (PBE0),[55,56] a range-separated functional with long-range-screened Hartree−Fock exchange (HSE),[57,58] and a range-separated functional with 100% Hartree−Fock exchange at long range (LC-ωPBE),[59] were used together with the TZVP basis set on the Co, Mn, Fe Cl, and N atoms and the SVP basis set on the C and H atoms.[60,61]

RESULTS AND DISCUSSION

Synthesis. The ligand *N*,*N*,*N*-tris(2-(2-pyridylamino)ethyl)-amine, or H$_3$(py$_3$tren), was obtained in one step by heating tren with 2-bromopyridine (3.14 equiv) and K$_2$CO$_3$ in DMSO (180 °C, 3 days). The slight excess of 2-bromopyridine was necessary to favor the complete formation of the tris-substituted product over the bis-substituted byproduct. The reaction worked well on a 20 g scale, and subsequent purification by column chromatography gave a moderate yield (14.2 g, 55%) of clean H$_3$(py$_3$tren) as a tan solid.

A five-membered series of homo- and heterobimetallic complexes featuring cobalt, iron, and/or manganese was then rapidly assembled using the two-step metalation strategy depicted in Scheme 1. Deprotonation of H$_3$(py$_3$tren) with 3 equiv of benzylpotassium (abbreviated as KBn) followed by metathesis with CoCl$_2$ and FeCl$_2$ generated the mononuclear precursors K[Co(py$_3$tren)] and K[Fe(py$_3$tren)], respectively. The crystal structure of K[Co(py$_3$tren)] shows that the cobalt center is exclusively coordinated by the tris(amido)amine donors, leaving the pyridine donors free to bind a second metal (SI Figure 7). Indeed, K[Co(py$_3$tren)] could be reacted with CoCl$_2$, FeCl$_2$(THF)$_{1.5}$, and MnCl$_2$(THF)$_2$ to form bimetallic

dx.doi.org/10.1021/ja409016w | J. Am. Chem. Soc. 2014, 136, 1842−1855

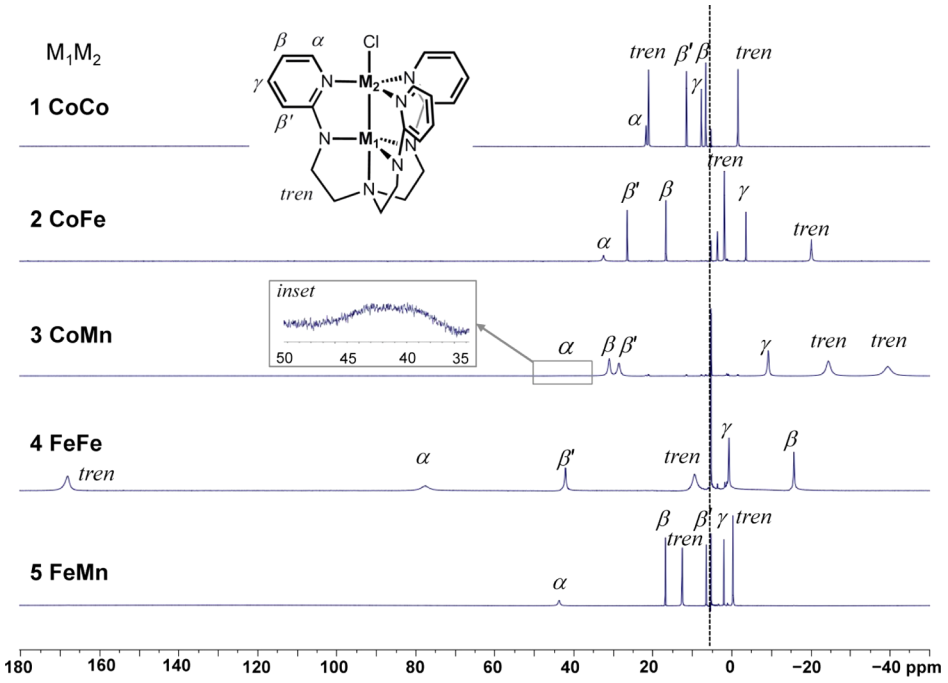

Figure 2. Stacked plot of the ^{1}H NMR spectra of **1**−**5** (500 MHz, CD_2Cl_2). The inset shows a close-up of a broad peak, assigned as the α proton in **3**. The residual solvent peaks are marked by the dotted line.

Table 2. Proton NMR Assignments of 1−5 with Chemical Shifts (δ) and T_1 Values

	δ/ppm (T_1/ms)				
compound	α	β	γ	β'	tren
1	21.7 (5.6)	6.7 (95)	7.7 (255)	11.5 (80)	20.9 (15), −1.6 (15)
2	32.5 (1.4)	16.8 (69)	−3.6 (105)	26.6 (46)	1.7 (33), −20.3 (29)
3	40.0 (nd)[a]	31.1 (1.9)	−9.2 (3.7)	28.6 (1.6)	−24.4 (1.3), −39.4 (1.1)
4	79 (nd)[a]	−15.7 (5.1)	0.78 (8.0)	42 (2.5)	168 (0.65), 9.5 (0.67)
5	43.7 (1.0)	16.8 (57)	2.0 (67)	6.5 (30)	−0.3 (16), 12.6 (7.8)

[a]nd = not determined because of peak broadness.

CoCoCl(py_3tren) (**1**), CoFeCl(py_3tren) (**2**), and CoMnCl(py_3tren) (**3**), respectively. Similarly, the mononuclear iron precursor K[Fe(py_3tren)] could be mixed with $FeCl_2(THF)_{1.5}$ and $MnCl_2(THF)_2$ to produce FeFeCl(py_3tren) (**4**) and FeMnCl(py_3tren) (**5**), respectively. The homobimetallic species **1** and **4** were synthesized at rt. On the other hand, the second metalations for the heterobimetallic complexes were conducted at much lower temperatures of −50 °C to impede metal scrambling in the two distinct binding sites (vide infra).

Of note, we did observe significant metal scrambling during the attempted synthesis of FeCoCl(py_3tren), which is a structural isomer of **2**. The metalation reaction of monoiron with $CoCl_2$ gave a mixture of dicobalt **1** and cobalt−iron **2** as determined by ^{1}H NMR analysis. In contrast, the metalation reaction of monocobalt with $FeCl_2(THF)_{1.5}$ proceeded quite cleanly to give **2**. On the basis of these results, we believe that complex **2** is the thermodynamically favored isomer and that attempts to kinetically prepare the higher-energy isomer were unsuccessful because of the lability of high-spin M(II) ions in these binding sites.

NMR Spectroscopy. Each of the five bimetallic compounds was characterized by NMR and UV−vis−NIR spectroscopy. The proton NMR spectra for all of the bimetallics contain six resonances, which is consistent with C_{3v} symmetry in solution (Figure 2). At rt, the complexes also appear to be paramagnetic on the basis of the isotropic peak shifts. Interestingly, dicobalt **1** has the smallest range of proton chemical shifts (−1.6 to 21.7 ppm), while diiron **4** has by far the largest range (−15.7 to 168 ppm).

The protons of the tren backbone can be distinguished from those of the pyridyl ring by the relative peak integrations of 2H and 1H, respectively. The pyridyl protons can be further differentiated by using two-dimensional NMR techniques. Correlation spectroscopy (COSY) of dicobalt **1** showed all of the major cross-peaks, including α−β, β−γ, and β'−γ (SI Figure 5). Unfortunately, the α−β cross-peak was not observed for cobalt−iron **2** or iron−manganese **5**, and *no* cross peaks were detected for **3** and **4**.

Since the loss of coupling information often accompanies paramagnetic peak broadening, we performed inversion recovery experiments to measure the spin−lattice relaxation times (T_1). The T_1 values and proton assignments are shown in Table 2. The α-protons of the pyridyl ring, which are the most downfield peak (except in the case of diiron **4**), have the shortest T_1 relaxation times among all of the proton types. At the other extreme, the γ-protons, which are located farthest from *any* metal center, have the longest T_1 values. The specific assignments of the β and β' protons are obvious in the case of **1** (based on COSY) but ambiguous for the other bimetallic complexes. As the β' proton is located closer to M_1 (4.5 to 4.6

dx.doi.org/10.1021/ja409016w | J. Am. Chem. Soc. 2014, 136, 1842−1855

Å) than β is to M_2 (~5.0 Å), we assign the resonance with the slightly shorter T_1 to β', which was independently confirmed for **1**. Interestingly, the bimetallic complexes can be subdivided into two categories based on their T_1 values: **1**, **2**, and **5** relax more slowly than **3** and **4**. It is also of interest that the faster relaxation times appear to be correlated with the overall spin state, $S_{tot} > {}^1/_2$ (vide infra), rather than the identity of the metal ion(s).

UV–Vis–NIR Spectroscopy. All of the coordination complexes, both mono- and dinuclear, are colorful. The mononuclear cobalt complex is bright green, and its bimetallic derivatives are green-brown for dicobalt **1**, red for cobalt–iron **2**, and green-yellow for cobalt–manganese **3**. In the iron series, the mononuclear iron species is yellow, while diiron **4** is dark red and iron–manganese **5** is orange.

Of interest, all of the complexes show intense bands in the UV–vis region and weak bands in the near-infrared region (NIR) (Figure 3). In the cobalt series, the mononuclear cobalt

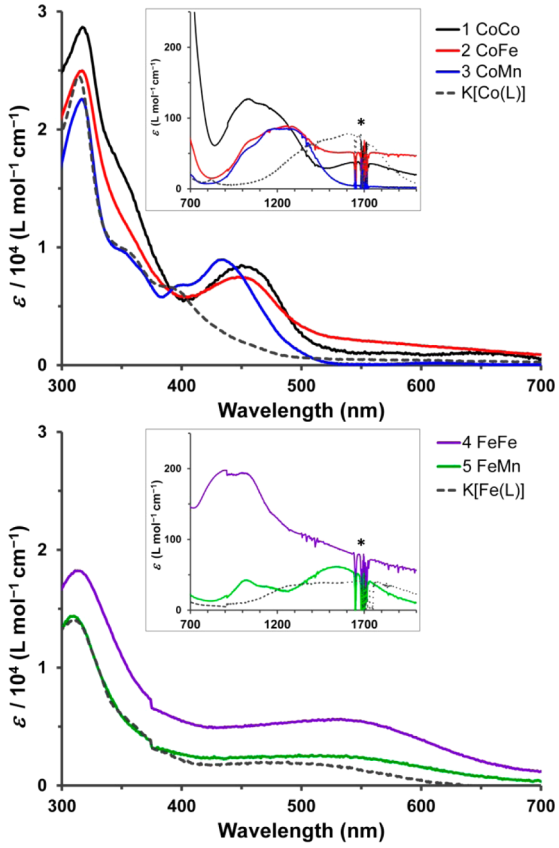

Figure 3. (top) UV–vis plots for K[Co(py$_3$tren)] and cobalt-containing complexes **1**–**3**. (bottom) UV–vis plots for K[Fe(py$_3$tren)] and iron-containing complexes **4** and **5**. The insets show the vis–NIR region. Spectra were collected from solutions in CH_2Cl_2. The asterisks denote artifacts from solvent subtraction.

complex and **1**–**3** have an intense peak at ~315 nm (ε > 22 000 M^{-1} cm^{-1}) with a shoulder at ~350 nm. A second shoulder is discerned for two of the complexes, the monocobalt (386 nm, ε = 6700 M^{-1} cm^{-1}) and cobalt–manganese (397 nm, ε = 6800 M^{-1} cm^{-1}). The bimetallics **1**–**3** also have a visible band at ~450 nm (ε = 7500–9000 M^{-1} cm^{-1}), which is notably absent for the monocobalt complex. Of interest, this band undergoes a blue shift in going from **1** (450 nm) to **2** (448 nm) to **3** (435 nm). This band could correspond to a metal-to-ligand charge transfer of the top metal (M_2). Related monometallic complexes with a trigonal pyridyl environment are known. For example, $[M(TPA)Cl]^+$ complexes, where TPA is tris(2-pyridylmethyl)amine), have been prepared for Co(II), Fe(II), and Mn(II).[62−64] However, in none of these cases was a peak near 450 nm with such high intensity reported. Alternatively, this band could correspond to a metal-to-metal charge transfer (MMCT), specifically Co → M_2, since the energy increases in going from M_2 = Co to Fe to Mn, which would be consistent with the trend in the metal ions' electronegativities. While the energy for MMCT may seem atypically high, transitions of d electrons from/into the M_1–M_2 σ/σ^* orbital would be expected to need higher-energy photons (vide infra). Finally, the monocobalt complex and **1**–**3** have NIR bands of similar intensity ($\varepsilon \approx 100$ M^{-1} cm^{-1}). The main NIR band shifts to the blue in going from the monocobalt complex to **2** ≈ **3** to **1**. The NIR band is thus proposed to arise from intrametal d–d transitions, though we cannot rule out intermetal d–d transitions (i.e., MMCT). Further work will be needed to make definitive assignments.

In the iron series, the UV–vis region is remarkably similar for the monoiron complex and the bimetallics **4** and **5**. Of note, the intensities of the bands in the UV–vis region are practically identical for the monoiron complex and iron–manganese **5** but are greater for diiron **4**, which suggests that the doubling of the intensity of the broad visible band may be due to the presence of two iron centers. The broad visible band is also detectably red-shifted in going from the monoiron complex to the bimetallics **4** and **5**. Unlike the cobalt series, there is no indication of any unique absorption feature that can be attributed to MMCT. Like the cobalt series, the NIR bands in the iron series also undergo a blue shift from the monoiron complex to bimetallics **4** and **5**, with the NIR band for homobimetallic diiron **4** gaining appreciable intensity.

X-ray Diffraction Studies. Single crystals of **1**–**5** were examined by X-ray diffraction. Dicobalt **1** crystallized in the orthorhombic space group $P2_12_12_1$, while complexes **2**–**5** all crystallized in the monoclinic space group $P2_1/n$ with similar unit cells. The coordination geometry at each metal center is trigonal-bipyramidal with an axial chloride ligand bound to the pyridine-coordinated metal (M_2) (Figure 4). Unfortunately, standard X-ray data cannot distinguish between metals with similar atomic numbers. To address the complicated issue of metal-site scrambling, we conducted X-ray anomalous scattering experiments for the heterobimetallic complexes (vide infra). Nonetheless, some clear trends are observed in the collective geometrical data that support the metal assignments (Table 3). For instance, the cobalt–apical amine (N_{ap}) bond distance remains essentially unchanged at 2.01 to 2.02 Å in the cobalt series (i.e., M_1 = Co). The iron–N_{ap} bond lengths in **4** and **5** are identical at 2.05 Å, and gratifyingly, they are slightly longer than those for Co–N_{ap}, which is consistent with the larger covalent radius of Fe(II) versus Co(II). Likewise, the bond distances between the bottom metal and the equatorial nitrogen atoms (i.e., M_1–N_{eq}) increase from 1.89–1.90 Å for M_1 = Co (in **1**–**3**) to 1.93–1.94 Å for M_1 = Fe (in **4** and **5**). For the metal–ligand bond lengths around the top metal center, especially M_2–Cl, no clear trend was readily discerned, as M_2 can be Co, Fe, or Mn. One notable finding is that when M_2 = Mn (in **3** and **5**), the M_2–N_{py} (where py = pyridine) and M_2–Cl bond distances are essentially identical.

Of central interest, the M_1–M_2 bond lengths would give insight into the nature of the metal–metal bonding in these

dx.doi.org/10.1021/ja409016w | J. Am. Chem. Soc. 2014, 136, 1842–1855

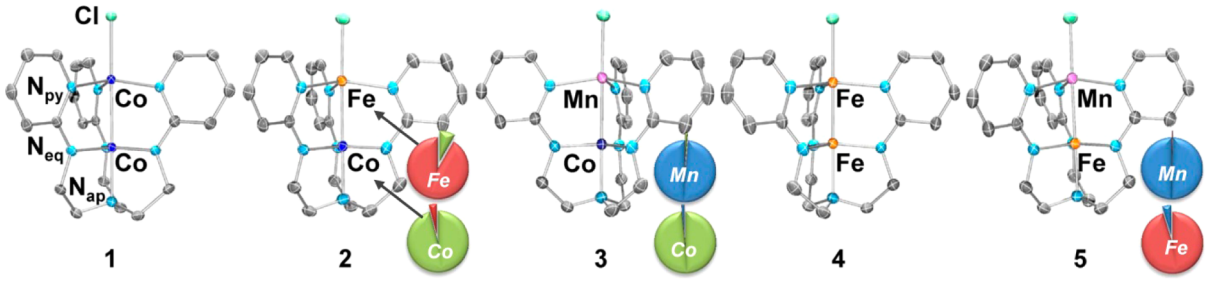

Figure 4. Solid-state structures of **1**–**5**. Thermal elliposids are shown at 50% probability. H atoms have been omitted for clarity. For the heterobimetallic species, the percentages of the two metals (Co in green, Fe in red, and Mn in blue) at each binding site (as determined by X-ray anomalous dispersion) are depicted as pie charts.

Table 3. Geometrical Parameters, Including Bond Lengths and Angles, for Complexes 1–5[a]

	1	2	3	4	5
M_1–M_2 (Å)	2.4986(4)	2.4913(3)	2.5312(4)	2.2867(5)	2.5283(3)
r[b]	1.08	1.07	1.09	0.98	1.08
M_1–N_{ap} (Å)	2.012(1)	2.010(1)	2.018(2)	2.054(1)	2.053(1)
M_1–N_{eq} (Å)[c]	1.885 ± 0.004	1.894 ± 0.006	1.903 ± 0.005	1.931 ± 0.007	1.940 ± 0.007
M_2–Cl (Å)	2.3487(5)	2.3455(4)	2.361(1)	2.3759(6)	2.3559(5)
M_2–N_{py} (Å)[c]	2.074 ± 0.007	2.107 ± 0.008	2.163 ± 0.008	2.11 ± 0.01	2.179 ± 0.007
M_1–M_2–Cl (deg)	177.69(2)	177.36(1)	177.92(2)	178.14(2)	177.26(2)

[a]Estimated standard deviations (esd's) are provided in parentheses. [b]r = ratio of the M_1–M_2 bond distance to the sum of the M_1 and M_2 single-bond radii. [c]The M_1–N_{eq} and M_2–N_{py} bond lengths are reported as averages ± standard deviations.

different metal pairs. The longest M_1–M_2 distances (2.53 Å) are observed in cobalt–manganese **3** and iron–manganese **5**. Intermediate metal–metal bond distances of 2.49–2.50 Å are found in dicobalt **1** and cobalt–iron **2**, while the diiron complex **4** has by far the shortest metal–metal bond distance in this series (2.29 Å). Because the expected differences in metal covalent radii complicate any absolute comparisons, Cotton et al. introduced the formal shortness ratio[65] (denoted as r in Table 3), where the metal–metal bond length is normalized by the sum of the two metals' single-bond radii. With the notable exception of diiron **4**, the r values for the other bimetallic complexes are significantly greater than 1 (1.07 to 1.09), suggesting that the metal–metal covalent interactions are weak at best. In the case of diiron **4**, the r value of 0.98 is near the expected value of 1.0 for a metal–metal single bond. Hence, diiron **4** is outstanding in this series in that it has a bona fide metal–metal bond. Of interest, an extremely short, isolable iron–iron bond of 2.13 Å was found in a diiron(I,I)–bis(guanidinate) complex by Jones and co-workers.[66] The authors proposed the iron centers to be multiply bonded and reported a large magnetic moment of 7.95μ_B.

The heterobimetallic species **2**, **3**, and **5** were investigated by X-ray anomalous scattering to assess the purity of each metal-binding site and consequently to determine the selectivity of our metalation strategy. This technique differentiates metals with similar numbers of electrons by exploiting the differences in the metals' K-edge energies. As the X-ray wavelength approaches the metal's K-edge energy, the anomalous terms of the atomic scattering factor change rapidly (Figure 1). With a synchrotron source, a series of anomalous data sets were collected to span the metals' K edges, including the edge energies (λ_{edge}) as well as 50 eV above and below it (λ_{edge} ± 50 eV).[67] In addition, an additional data set was collected at high energy (30 keV) to determine a high-resolution structure. For reasons detailed in the Experimental Section, the measurements taken at lower energy ($\lambda > \lambda_{edge}$) are more reliable, so they were used exclusively in determining the metal occupancies at each binding site.[37] Recently, Betley and co-workers reported a similar methodology.[22] A unique aspect of our approach is that we simultaneously analyzed the anomalous data sets and performed a least-squares refinement[38] to determine the metal occupancies.

The high-resolution structures of the heterobimetallic complexes are practically identical (within 0.01 Å) to those determined by standard X-ray diffraction (SI Tables 2 and 3). The results for the metal occupancies are given in Table 4 and graphically portrayed as pie charts in Figure 4. Gratifyingly, very little metal mixing was observed. For compounds **3** and **5**, both metal-binding sites are substitutionally pure (≥95%), and thus, we expect these complexes to be highly homogeneous. While the main component is quite clearly the expected product, $M_1M_2Cl(py_3tren)$, other related species may be present as minor impurities, including the constitutional isomer $M_2M_1Cl(py_3tren)$ and the two homobimetallic species. If we assume statistical mixing of the M_1 and M_2 populations at the two

Table 4. Metal Compositions (Co, Fe, Mn) at the Unique Binding Sites (M_1, M_2) in the Heterobimetallic Complexes 2, 3, and 5 As Determined by X-ray Anomalous Scattering Studies

compound	M_1	M_2	purity (%)	M_1:M_2[a]
2	Co 0.957(11) Fe 0.043(11)	Fe 0.916(11) Co 0.084(11)	88	Co:Fe 1.04:0.96 (1.01:0.99)
3	Co 0.983(12) Mn 0.017(12)	Mn 0.985(11) Co 0.015(11)	97	Co:Mn 1.00:1.00 (0.99:1.01)
5	Fe 0.952(16) Mn 0.048(16)	Mn 0.995(15) Fe 0.005(15)	95	Fe:Mn 0.96:1.04 (0.92:1.08)

[a]Metal ratios of the *bulk* samples as determined by ICP-OES are given in parentheses.

dx.doi.org/10.1021/ja409016w | J. Am. Chem. Soc. 2014, 136, 1842–1855

independent sites, then the overall purities of $M_1M_2Cl(py_3tren)$ are estimated to be 97 and 95% for **3** and **5**, respectively. The same analysis shows complex **2** to have an overall purity of 88% with a significant presence of dicobalt **1** (8%). This suggests that either dicobalt **1** is carried over from the first metalation step and/or that iron and cobalt ions exchange during the second metalation. Because of the high purity of the related cobalt-containing complex **3**, we conclude that it is the mixing of the similar iron and cobalt centers during the second metalation in the synthesis of **2** that generates the dicobalt impurities. While these results are promising for single crystals, they do not assess the purity of the bulk materials. Hence, we sought to independently verify the metal composition of the bulk using ICP-OES. The metal compositions are in excellent agreement with those determined by the anomalous measurements (Table 4, last column).

Electrochemistry. All of the bimetallic coordination complexes were characterized by cyclic voltammetry in 0.1−0.4 M $[n\mathrm{Bu_4N}]PF_6$/THF. To aid the interpretation of the cyclic voltammograms (CVs), we also examined the neutral ligand and the monometallic complexes. The ligand, $H_3(py_3tren)$, shows an irreversible oxidation at E_{pa} = 0.5 V (SI Figure 6), which shifts cathodically to 0.2 and −0.2 V for the monoiron and monocobalt complexes, respectively. The mononuclear species also have an additional quasi-reversible oxidation at −0.5 V for cobalt and −1.4 V for iron, where the monoiron complex is significantly easier to oxidize than the monocobalt species by nearly 1 V (SI Figure 6). No reductive processes were observed for $H_3(py_3tren)$ or the monometallic species.

The CVs of the bimetallic complexes are shown in Figure 5, and the corresponding redox potentials are given in Table 5.

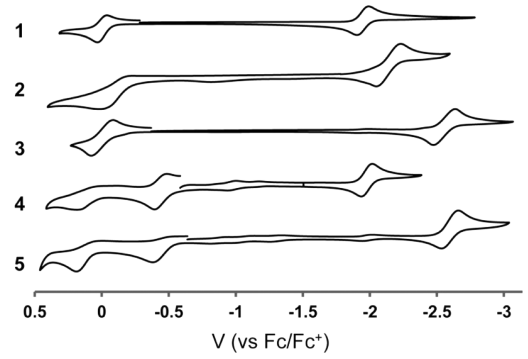

Figure 5. Cyclic voltammograms of **1**−**5** in 0.4 M $[n\mathrm{Bu_4N}]PF_6$/THF at 300 mV/s (except for **2**, 0.1 M $[n\mathrm{Bu_4N}]PF_6$/THF at 10 mV/s).

Complexes **1**−**5** all show an irreversible oxidation at E_{pa} = 0.41 to 0.50 V, which is attributed to a ligand-based oxidation (not shown in the figure). In the cobalt series, complexes **1**, **2**, and **3** all have one quasi-reversible/irreversible oxidative process at $E^{\circ\prime}/E_{pa}$ = 0.0 V. Because of the similarity in the redox potentials of the monocobalt complex and the cobalt series, the redox reaction occurring at 0 V is likely to be Co(II)/Co(III) in nature. The iron series, consisting of **4** and **5**, differ from the cobalt series in that two additional oxidative processes are observed at $E^{\circ\prime}/E_{pa}$ = −0.40 and 0.19 V, which are significantly different from the monoiron results. Presumably, the former redox potential corresponds to an Fe(II)/Fe(III) couple. In related work, Nippe and Berry[68] showed that even a weak $Cr_2\cdots Fe$ interaction can significantly perturb the Fe(II)/Fe(III) redox potential. The second redox couple can be attributed to either M_2(II)/M_2(III) or perhaps even further oxidation to Fe(IV). Strangely, M_2(II)/M_2(III) redox couples were not observed in the cobalt series, and Fe(III)/Fe(IV) redox couples can be as low as 0.25 V vs Fc/Fc^+ with tris(amido)amine ligands.[69] On the other hand, the monoiron complex showed no indication of a second iron-based oxidation.

Table 5. Reduction and Oxidation Potentials of 1−5[a]

compound	oxidations ($E^{\circ\prime}/E_{pa}$)[b]	reduction ($E^{\circ\prime}$)
1	−0.01, *0.48*	−1.95
2	−0.04, 0.41	−2.06
3	0.00, *0.49*	−2.55
4	−0.45, 0.19, 0.44	−1.98
5	−0.39, 0.19, 0.50	−2.61

[a]Values are given in V vs Fc/Fc^+. [b]E_{pa} values are denoted in italics.

Each of complexes **1**−**5** exhibits a single quasi-reversible/reversible reductive process. Because of the lack of any similar processes in the monometallic species, we believe that these reductions are localized at the top metal (i.e., M_2). In support of this hypothesis, when M_2 = Mn as in cobalt−manganese **3** and iron−manganese **5**, the reduction potentials are nearly identical at −2.6 V. Also, in the cobalt series, the reduction potentials shift as a function of M_2, from −1.95 V for **1** (M_2 = Co) to −2.06 V for **2** (M_2 = Fe) to −2.55 V for **3** (M_2 = Mn). While these potentials correspond to the one-electron M(II)/M(I) redox couples, they follow the same trend as the two-electron redox potentials for the M(II) ions, where $M(II)(aq) + 2e^- \rightarrow M(s)$. However, when M_2 = Fe, the reduction potentials are slightly different for **2** (−2.06 V) and **4** (−1.98 V). Perhaps this difference arises from the dissimilarity of the metal−metal interactions in **2** versus **4**, where the latter has a more delocalized metal−metal bond compared with the former.

To summarize the CV studies, bimetallic complexes **1**−**5** can undergo multiple electron transfers, and these reactions appear to be primarily localized at the individual metal centers. Specifically, the first oxidative processes are associated with M_1, and their potentials correspond to those of M_1(II)/M_1(III) redox couples. The potentials of the reductive processes, on the other hand, change with M_2 and are consistent with the M_2(II)/M_2(I) redox couples.

Mössbauer Spectroscopy. The iron-containing bimetallic complexes were further characterized by ^{57}Fe Mössbauer spectroscopy (0 T, 80 K). As expected, one major doublet was observed for the heterobimetallic compounds **2** and **5**, while two main signals were observed for diiron **4**, which is consistent with its two unique iron sites (Figure 6 and Table 6). In cobalt−iron **2**, the iron center has an isomer shift (δ) of 0.88 mm/s with a quadrupole splitting (ΔE_Q) of 2.62 mm/s. These parameters are typical of mononuclear high-spin Fe(II). However, in iron−manganese **5**, both δ and ΔE_Q have significantly decreased to 0.46 and 1.69 mm/s, respectively. A similar decrease in isomer shift was observed for both iron centers in diiron **4** (δ = 0.58 and 0.48 mm/s). Although these isomer shifts are atypically low for S = 2 Fe(II) centers, they are also unusually high for either S = 1 or S = 0 Fe(II). In the literature, decreased isomer shifts have been reported for systems where the iron center is engaged in metal−metal bonding. For example, trigonal diiron(II,II) complexes with iron−iron distances ranging from 2.58 to 2.87 Å have isomer shift values of ∼0.60 mm/s.[34] A triiron(II,II,II) system with short metal−metal bond distances of 2.30 Å (comparable to **4**)

dx.doi.org/10.1021/ja409016w | J. Am. Chem. Soc. 2014, 136, 1842−1855

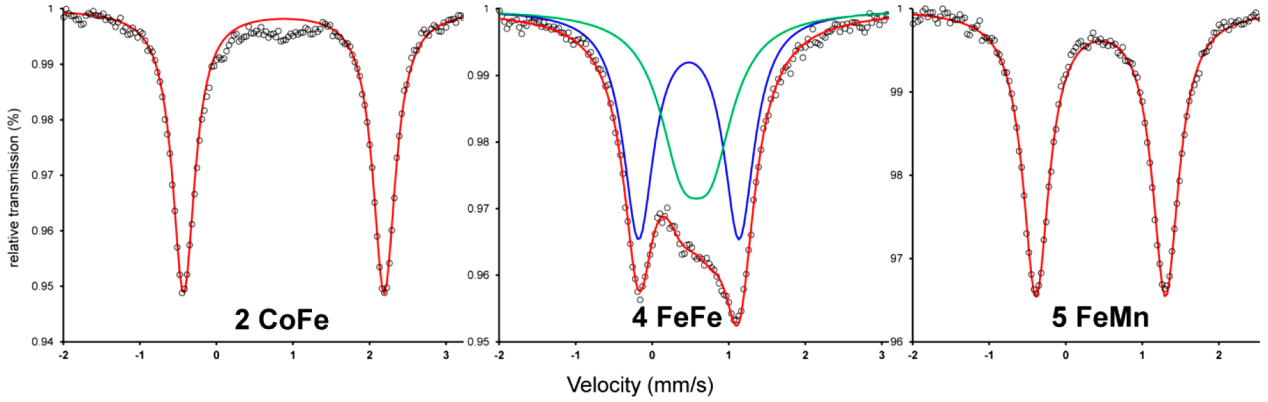

Figure 6. Zero-field Mössbauer spectra of (left) **2**, (center) **4**, and (right) **5** at 80 K. The experimental data are plotted as dots. Total fits are shown as red lines. The Mössbauer parameters δ (ΔE_Q) in mm/s are as follows: for **2**, 0.88 (2.62); for **4**, 0.58 (0.38) (in green) and 0.48 (1.31) (in blue); for **5**, 0.46 (1.69).

Table 6. Zero-Field ^{57}Fe Mössbauer Parameters (in mm/s) for 2, 4, and 5

compound	δ	ΔE_Q	line width[a]
2	0.88	2.62	0.35
4	0.58	0.38	0.72
	0.48	1.31	0.48
5	0.46	1.69	0.42

[a]Modeled as two Lorentzian lines with equal intensities and widths.

has an even lower isomer shift of 0.38 mm/s, although this could also be attributed to the overall lower spin (S = 1).[70]

For diiron **4**, the two Mössbauer signals can be tentatively assigned by comparison to those of **5**. Specifically, the doublet centered at 0.48 mm/s in complex **4** is remarkably similar to that of **5**. Since **4** and **5** have a common iron site at M_1, we believe that this doublet for **4** corresponds to M_1 and that the other signal at 0.58 mm/s belongs to M_2. Although complexes **2** and **4** share a common iron site at the M_2 position, their isomer shift values are dramatically different, and this variation may be attributed to the significant metal−metal bonding in **4** that is not present in **2**.

Magnetic Susceptibility. We conducted variable-temperature magnetic susceptibility measurements of the bimetallic complexes **1**−**5** under an applied dc field of 1 T. The magnetic susceptibility (χ) data are plotted in Figure 7 as χT versus T, where T is the absolute temperature. All of the χT plots show a temperature dependence and appear to reach ground-state configurations in the low-temperature range of 15 to 50 K. Below 15 K, changes in χT may arise from several factors, including field saturation, magnetic anisotropy, and/or intermolecular effects. As we were primarily interested in understanding the metal−metal exchange interactions, which are evident at higher T, no additional measurements were made to elucidate the factors that manifest themselves in the temperature regime below 15 K.

At low T (from 15 to 50 K), χT approaches 0 for dicobalt **1**, indicating a singlet ground state. For cobalt−iron **2** and iron−manganese **5**, χT plateaus at 0.36 and 0.45 cm^3 K/mol, respectively, at low T. These values are near 0.375 cm^3 K/mol, the expected value for $S = {}^1/_2$. For cobalt−manganese **3**, χT decreases slowly to 0.95 cm^3 K/mol at low T, which is consistent with S = 1 (for g = 2, χT = 1.0 cm^3 K/mol). One general explanation is that the ground spin states are the net outcome of two high-spin M(II) spins that are antiferromagnetically coupled, where the overall spin state, S_{tot}, is equivalent to $S_1 - S_2$. Thus, when the two M(II) ions are both cobalt as in **1**, a singlet state is generated. When the two M(II) ions belong to neighboring groups of the periodic table, as in **2** and **5**, a doublet spin state results. Finally, a triplet state is derived for **3**, where the group numbers of the two M(II) ions differ by two.

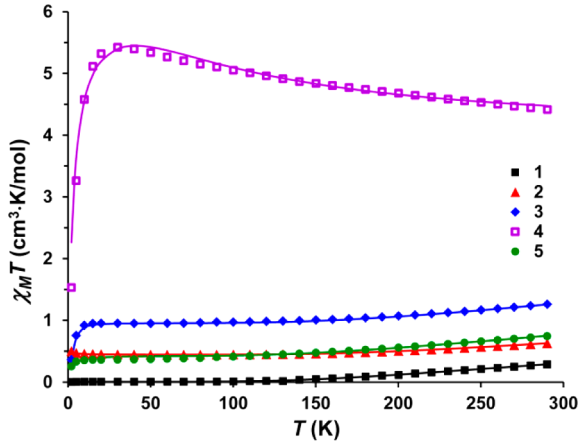

Figure 7. Temperature dependence of the magnetic susceptibility, plotted as $\chi_M T$, of **1** (black solid squares), **2** (red triangles), **3** (blue diamonds), **4** (purple open squares), and **5** (green circles) at 1 T from 2 to 290 K. Solid lines represent best fits (see Table 7 for the simulation parameters).

For **1**, **2**, **3**, and **5**, χT rises slightly with increasing temperature. The increase in χT suggests thermal population of higher spin states, which likely arise from the reduced coupling of the two high-spin M(II) centers. By using a two-spin Hamiltonian to simulate the magnetic data, we determined the average g values and antiferromagnetic exchange coupling constants (J) for these various metal−metal interactions. These parameters are provided in Table 7. We found that the magnitude of the coupling constant decreases significantly (>50 cm^{-1}) in going from dicobalt **1** to cobalt−iron **2** to iron−manganese **5**, with a smaller decrease of 25 cm^{-1} in going to cobalt−manganese **3**.

Notably, diiron **4** stands apart from the other members in that it exhibits higher χT values, peaking to 5.42 cm^3 K/mol at 30 K. This value is near the spin-only value for S = 3 (χT = 6.0 cm^3 K/mol). Coincidentally, a χT value of 6.0 cm^3 K/mol is also expected for two noninteracting S = 2 spins [e.g., high-spin

dx.doi.org/10.1021/ja409016w | J. Am. Chem. Soc. 2014, 136, 1842−1855

Table 7. Magnetic Couplings, Anisotropy Constants, and *g* Values of 1−5[a]

compd	S_{tot}	S_1	S_2	J (cm^{-1})	g_1	g_2	$D_{1,2}$ (cm^{-1})[b]	θ_w (K)[b]
1	0	1.5	1.5	−231	2.16	2.16	0	0
2	0.5	1.5	2.0	−184	2.00	2.09	0	0.3
3	1.0	1.5	2.5	−120	2.06	2.00	2.5[c]	0
4[d]	*3.0*	*2.0*	*1.0*	*+14*	*2.00*	*2.00*	*0*	*−3.0*
5	0.5	2.0	2.5	−145	2.00	2.06	0	−1.5

[a]Some spectra were corrected for temperature-independent paramagnetism (TIP). See the Experimental Section. [b]As discussed in the text, we cannot differentiate between magnetic anisotropy arising from zero-field splitting (D) or intermolecular interactions (θ_w) below 15 K, so these values are not well parametrized. [c]D_1 and D_2 were arbitrarily set to be equal. [d]Parameters were obtained by imposing a *localized* treatment, though we propose that a *delocalized* treatment is more appropriate for **4**.

Fe(II)]. However, the latter interpretation is inconsistent with the temperature dependence of χT, which decreases with increasing temperature. It is further improbable that **4** should have noninteracting spins when it is the only complex in this series with a bona fide metal−metal bond. Therefore, the magnetic data suggest a very different type of magnetic interaction in **4**.

The magnetic behavior of complexes featuring multiple metal centers can be complex, as several exchange mechanisms are possible, including direct exchange (via metal−metal), superexchange (via a bridging ligand), and double exchange. Double-exchange pathways, which may occur in mixed-valent systems, are easily ruled out in these systems since the metal ions are in the same oxidation states of +2. While some of the heterobimetallic systems (e.g., cobalt−iron **2**) may superficially resemble mixed-valent systems (with a d^7−d^6 electron count), it would be unreasonable for an electron to move between the metal ions as the resulting d^6−d^7 configuration would formally correspond to Co(III)−Fe(I).

In systems featuring weak metal−metal interactions, direct and superexchange pathways can compete. With the exception of **4**, the metal ions in these bimetallic systems couple antiferromagnetically. We conclude at this stage that the primary pathway is superexchange. Our reasoning is based on the fact that the metal−metal interactions in complexes **1**, **2**, **3**, and **5** are weak at best. If direct exchange were dominant, then complex **4**, which should have the best d−d orbital overlap, should strongly couple antiferromagnetically, which is not observed. Moreover, the Goodenough−Kanamori rules predict that single electrons occupying d orbitals of δ symmetry with respect to the M−M axis would couple antiferromagnetically through the π system of the pyridyl−amide bridge. On the other hand, it is not obvious how single electrons occupying d orbitals of π symmetry would interact (as there are no matching orbitals on the ligand), so it is possible that direct exchange via a weak metal−metal interaction may also play a significant role in the overall antiferromagnetism.

In the case of **4**, we have scrutinized similar exchange interactions, but no satisfactory model has yet emerged. For instance, we considered **4** as two localized spins that couple ferromagnetically. To obtain a good fit of the experimental data and in order to produce S_{tot} = 3, one of the iron centers was set to high-spin Fe(II) while the other had to be modeled as intermediate-spin Fe(II). A weak ferromagnetic coupling of +14 cm^{-1} was thus determined (Table 7). The fit, however, is problematic because we cannot explain the origin of the different spins of the two Fe(II) centers. We also considered an alternative fit with two equal $S = {}^3/_2$ centers, but to maintain the +4 charge of the diiron core, the oxidation states would have to be different, namely, Fe(III)Fe(I). The failure of the localized models is not surprising in light of the work by Betley and co-workers,[23] who have described the shortcomings of the localized description for explaining the magnetic behavior of systems with strong metal−metal interactions. Instead, they advocate the use of a delocalized molecular orbital (MO) scheme to account for the temperature variation of χT. Basically, metal d orbitals that engage in metal−metal bonding give rise to a delocalized d-orbital manifold that by population according to Hund's rules yields higher-spin ground states. In the delocalized model, the decrease in χT would result from spin crossover to a lower spin state.

Theoretical Studies. To validate our hypothesis of delocalized metal−metal bonding in **4**, we performed multiconfigurational calculations on the full experimental structures

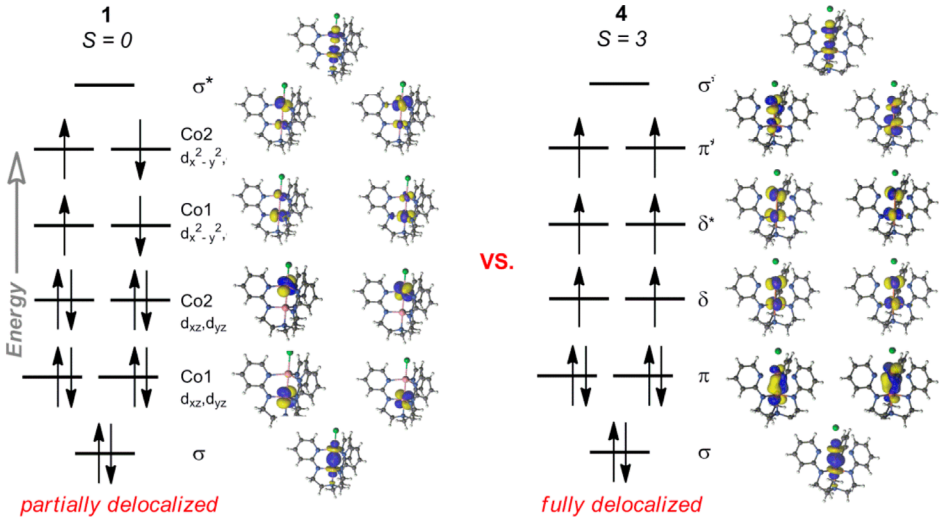

Figure 8. Qualitative MO diagrams showing the natural orbitals for (left) dicobalt **1** and (right) diiron **4**. Only the dominant electronic configurations are shown.

dx.doi.org/10.1021/ja409016w | J. Am. Chem. Soc. 2014, 136, 1842−1855

of compounds **1**–**5** using the CASSCF method followed by CASPT2 calculations to recover additional dynamical correlation. For each compound, the active space comprised 12 orbitals, including all 10 valence 3d orbitals and two additional 4d orbitals that correlated with the 3d orbitals. The energies of various spin states were computed, and with the exception of **4**, the calculated ground states matched the experimentally determined states (SI Table 4). To correctly predict the ground state of **4**, we investigated a much larger active space of 20 orbitals (all of the 3d and 4d orbitals) with RAS SCF and PT2 calculations. Although the singlet state was still preferred, the energy difference between the singlet and septet states was minimal (<3 kcal/mol).

For metal–metal bonds in trigonal symmetry, the maximum overlap of the two metals' 3d orbitals would ideally yield a highly delocalized MO manifold with σ, π, and δ bonds, such as $(\sigma)(\pi)(\delta)(\delta^*)(\pi^*)(\sigma^*)$. Poor overlap of the metal orbitals, however, would cause electron density to be localized at the individual metal centers. The heterobimetallic species are expected to have greater localization than the homobimetallics because different metal centers should have worse overlap compared with identical metal centers. Thus, it is interesting that dicobalt **1** is low-spin and shares similar characteristics with the heterobimetallic species whereas diiron **4** is higher-spin and the lone standout. To elucidate the physical bases of their different properties, the bonding natures of **1** and **4** were further investigated.

The main electronic configurations of **1** and **4** are compared in Figure 8. Of note, the MO diagram of **4** shows the idealized metal–metal bond that is fully delocalized. The main electronic configuration of **4**, which accounts for 28% of the total wave function, is $(\sigma)^2(\pi)^4(\delta)^2(\delta^*)^2(\pi^*)^2(\sigma^*)^0$. The septet state thus arises from the population of energetically close δ, δ^*, and π^* MOs. This configuration also corresponds to a formal double bond between the iron centers. However, the sum of all the contributing configurations yields MOs with the following natural populations, $(\sigma)^{1.27}(\pi)^{3.42}(\delta)^{2.01}(\delta^*)^{1.99}(\pi^*)^{2.52}(\sigma^*)^{0.72}$, where the increased population in the π^* and σ^* antibonding orbitals lowers the effective bond order (EBO) to 0.73, which is reasonably close to a single bond.

In contrast, complex **1** is characterized by a significantly more localized MO diagram, where the only truly delocalized natural orbitals are σ and σ^*. (The δ-symmetry MOs are predominantly localized at one metal center, as the ratio of the electron densities of the two cobalt centers ranges from 5:1 to 9.5:1). The main electronic configuration of **1**, which accounts for 19% of the total wave function, is $(\sigma)^2(\mathrm{Co_1}\ d_{yz},d_{xz})^4(\mathrm{Co_2}\ d_{yz},d_{xz})^4(\mathrm{Co_1}\ d_{xy},d_{x^2-y^2})^2(\mathrm{Co_2}\ d_{xy},d_{x^2-y^2})^2(\sigma^*)^0$. Formally, this configuration predicts a single bond between the cobalt centers. Again, however, the sum of all the configurations, $(\sigma)^{1.22}(\mathrm{Co_1}\ d_{yz},d_{xz})^{3.98}(\mathrm{Co_2}\ d_{yz},d_{xz})^{3.96}(\mathrm{Co_1}\ d_{xy},d_{x^2-y^2})^{2.08}(\mathrm{Co_2}\ d_{xy},d_{x^2-y^2})^2(\sigma^*)^{0.78}$, provides an EBO of only 0.22, which is consistent with a metal–metal interaction that is weaker than a single bond.

For all of the heterobimetallic complexes **2**, **3**, and **5**, the ground states were predicted to be highly multiconfigurational, where the main electronic configuration accounts for only 7% or less of the total wave function (SI Table 5). Thus, the "main" configurations for the heterobimetallics are not representative of the whole bonding picture, so we will not delve further into their bonding descriptions. One important finding, however, is that the EBOs are all low, between 0.22 and 0.31 (SI Table 5), which is consistent with the long metal–metal bond lengths observed experimentally.

Finally, density functional theory (DFT) calculations were performed to shed light on the magnetic interactions between the metal centers within the bimetallic complexes. Magnetic coupling constants can be extracted from DFT solutions of the high-spin and broken-symmetry states, which were calculated with three different exchange-correlation functionals: PBE0, HSE, and LC-ωPBE (Table 8). For "purely" magnetic systems,

Table 8. Calculated Magnetic Coupling Constants J (in cm^{-1}) Obtained Using Various Functionals

compound	PBE0	HSE	LC-ωPBE	J_{exp}
1	−333	−350	−370	−231
2	−207	−244	−304	−184
3	−210	−217	−231	−120
5	−181	−187	−198	−145

where the magnetic electrons are localized at the individual metal centers, the HSE and LC-ωPBE functionals typically give more accurate coupling values compared with PBE0.[71,72] For bimetallic **1**, **2**, **3**, and **5**, the calculated magnetic coupling values were fairly consistent across the functionals. In contrast, the computed magnetic couplings for diiron **4** were quite inconsistent for the various functionals, and thus, compound **4** was excluded from the present study. Although the predicted magnetic coupling constants were generally overestimated, the *trend* in the $|J|$ values (Figure 9) shows a good correspondence

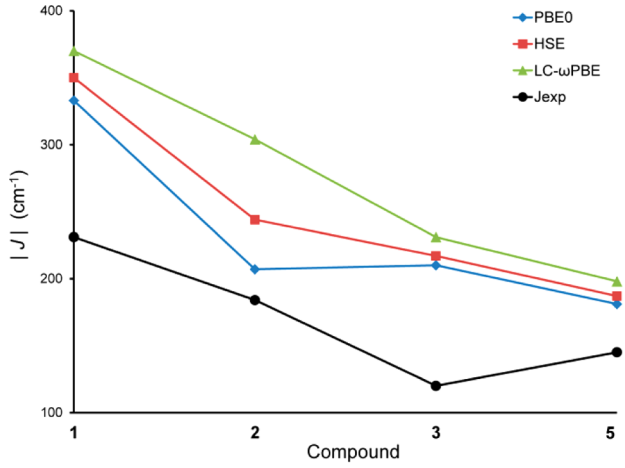

Figure 9. Plot of $|J|$ values for compounds **1**, **2**, **3**, and **5**.

between theory and experiment, especially for LC-ωPBE. All of the functionals correctly reproduce an important periodic trend for the cobalt series, namely, that the antiferromagnetic coupling decreases in the CoM_2 complexes in going from M_2 = Co to Fe to Mn. One discrepancy between theory and experiment is that a weaker coupling is predicted for **5** than for **3** rather than vice versa. We hypothesize that this discrepancy arises from a problem with electron correlation, which can become even more complicated when magnetic orbitals overlap. Thus, there is still room for the development of new and more generally applicable exchange–correlation functionals for computing isotropic magnetic couplings.

dx.doi.org/10.1021/ja409016w | J. Am. Chem. Soc. 2014, 136, 1842–1855

CONCLUSIONS

A simple ligand design has allowed the preparation of bimetallic complexes containing Mn(II), Fe(II), and/or Co(II) ions with high compositional purity. Gratifyingly, minute disorder resulting from metal mixing was observed, despite the fact that these metal ions are typically substitutionally labile and share similar covalent radii. Three heterobimetallic complexes (CoMn, CoFe, and FeMn) were isolated and are highly substitutionally pure in the two metal-binding sites. With these different metal−metal pairings in hand, we were able to characterize their spectroscopic, electronic, and magnetic properties. We do not yet understand why the diiron complex is an outlier of this series, but we correlate its short metal−metal bond and higher spin state with a more delocalized electron density between the two metal centers. Future efforts will focus on exchanging the chloride ligand with more reactive groups in order to study the effects of the metal−metal bonding on the reactivity.

ASSOCIATED CONTENT

Supporting Information

Additional NMR spectra, CV and X-ray crystallography details, and computational data. This material is available free of charge via the Internet at http://pubs.acs.org.

AUTHOR INFORMATION

Corresponding Authors

ebill@gwdg.de
gagliard@umn.edu
clu@umn.edu

Notes

The authors declare no competing financial interest.

ACKNOWLEDGMENTS

Andreas Göbels and Bernd Mienert are acknowledged for assisting with the acquisition of spectroscopic data. S.J.T. and C.C.L. thank Prof. Dave Blank for the use of his UV−vis−NIR instrument and Prof. Larry Que for insightful discussions. C.C.L. thanks Prof. John Berry (University of Wisconsin, Madison) for sharing his ideas. X-ray diffraction experiments were performed using a crystal diffractometer acquired through NSF-MRI Award CHE-1229400. ICP-OES measurements and analysis were carried out by Rick Knurr at the Characterization Facility, University of Minnesota, which receives partial support from National Science Foundation (NSF) through the MRSEC Program. The synthetic work was supported by NSF (CHE-1254621) and the Alfred Sloan Foundation (C.C.L.). Computing support and resources were provided by the Minnesota Supercomputing Institute. The computational results (R.K.C., R.M., H.J.K., L.G.) are based on work supported by the NSF (CHE-1212575). ChemMatCARS Sector 15 is principally supported by NSF/DOE (CHE-0822838). Use of the Advanced Photon Source was supported by the U.S. Department of Energy (DOE), Office of Science, Office of Basic Energy Sciences, under Contract DE-AC02-06CH11357.

REFERENCES

(1) *Biological Inorganic Chemistry: Structure and Reactivity*; Bertini, I., Gray, H. B., Stiefel, E. I., Valentine, J. S., Eds.; University Science Books: Sausalito, CA, 2007.
(2) Fontecilla-Camps, J. C.; Volbeda, A.; Cavazza, C.; Nicolet, Y. *Chem. Rev.* **2007**, *107*, 4273.
(3) Ragsdale, S. W. *J. Inorg. Biochem.* **2007**, *101*, 1657.
(4) Dobbek, H.; Svetlitchnyi, V.; Gremer, L.; Huber, R.; Meyer, O. *Science* **2001**, *293*, 1281.
(5) Kung, Y.; Drennan, C. L. *Curr. Opin. Chem. Biol.* **2011**, *15*, 276.
(6) Jiang, W.; Yun, D.; Saleh, L.; Barr, E. W.; Xing, G.; Hoffart, L. M.; Maslak, M.-A.; Krebs, C.; Bollinger, J. M., Jr. *Science* **2007**, *316*, 1188.
(7) Jiang, W.; Bollinger, J. M., Jr.; Krebs, C. *J. Am. Chem. Soc.* **2007**, *129*, 7504.
(8) Stubbe, J.; Nocera, D. G.; Yee, C. S.; Chang, M. C. Y. *Chem. Rev.* **2003**, *103*, 2167.
(9) Dassama, L. M. K.; Boal, A. K.; Krebs, C.; Rosenzweig, A. C.; Bollinger, J. M. *J. Am. Chem. Soc.* **2012**, *134*, 2520.
(10) Roos, K.; Siegbahn, P. E. M. *Biochemistry* **2009**, *48*, 1878.
(11) Andersson, C. S.; Öhrström, M.; Popović-Bijelić, A.; Gräslund, A.; Stenmark, P.; Högbom, M. *J. Am. Chem. Soc.* **2012**, *134*, 123.
(12) Han, W.-G.; Giammona, D. A.; Bashford, D.; Noodleman, L. *Inorg. Chem.* **2010**, *49*, 7266.
(13) Younker, J. M.; Krest, C. M.; Jiang, W.; Krebs, C.; Bollinger, J. M., Jr.; Green, M. T. *J. Am. Chem. Soc.* **2008**, *130*, 15022.
(14) Sano, Y.; Weitz, A. C.; Ziller, J. W.; Hendrich, M. P.; Borovik, A. S. *Inorg. Chem.* **2013**, *52*, 10229.
(15) Carboni, M.; Latour, J.-M. *Coord. Chem. Rev.* **2011**, *255*, 186.
(16) Carboni, M.; Clémancey, M.; Molton, F.; Pécaut, J.; Lebrun, C.; Dubois, L.; Blondin, G.; Latour, J.-M. *Inorg. Chem.* **2012**, *51*, 10447.
(17) Jarenmark, M.; Haukka, M.; Demeshko, S.; Tuczek, F.; Zuppiroli, L.; Meyer, F.; Nordlander, E. *Inorg. Chem.* **2011**, *50*, 3866.
(18) Holman, T. R.; Wang, Z.; Hendrich, M. P.; Que, L., Jr. *Inorg. Chem.* **1995**, *34*, 134.
(19) Hotzelmann, R.; Wieghardt, K.; Flörke, U.; Haupt, H.-J.; Weatherburn, D. C.; Bonvoisin, J.; Blondin, G.; Girerd, J.-J. *J. Am. Chem. Soc.* **1992**, *114*, 1681.
(20) Ross, S.; Weyhermüller, T.; Bill, E.; Bothe, E.; Flörke, U.; Wieghardt, K.; Chaudhuri, P. *Eur. J. Inorg. Chem.* **2004**, 984.
(21) Borovik, A. S.; Que, L., Jr.; Papaefthymiou, V.; Münck, E.; Taylor, L. F.; Anderson, O. P. *J. Am. Chem. Soc.* **1988**, *110*, 1986.
(22) Powers, T. M.; Gu, N. X.; Fout, A. R.; Baldwin, A. M.; Hernández Sánchez, R.; Alfonso, D. M.; Chen, Y.-S.; Zheng, S.-L.; Betley, T. A. *J. Am. Chem. Soc.* **2013**, *135*, 14448.
(23) Eames, E. V.; Harris, T. D.; Betley, T. A. *Chem. Sci.* **2012**, *3*, 407.
(24) Eames, E. V.; Hernández Sánchez, R.; Betley, T. A. *Inorg. Chem.* **2013**, *52*, 5006.
(25) Fout, A. R.; Xiao, D. J.; Zhao, Q.; Harris, T. D.; King, E. R.; Eames, E. V.; Zheng, S.-L.; Betley, T. A. *Inorg. Chem.* **2012**, *51*, 10290.
(26) Tsui, E. Y.; Tran, R.; Yano, J.; Agapie, T. *Nat. Chem.* **2013**, *5*, 293.
(27) Tsui, E. Y.; Agapie, T. *Proc. Natl. Acad. Sci. U.S.A.* **2013**, *110*, 10084.
(28) Rudd, P. A.; Liu, S.; Gagliardi, L.; Young, V. G., Jr.; Lu, C. C. *J. Am. Chem. Soc.* **2011**, *133*, 20724.
(29) Rudd, P. A.; Liu, S.; Planas, N.; Bill, E.; Gagliardi, L.; Lu, C. C. *Angew. Chem., Int. Ed.* **2013**, *52*, 4449.
(30) Clouston, L. J.; Siedschlag, R. B.; Rudd, P. A.; Planas, N.; Hu, S.; Miller, A. D.; Gagliardi, L.; Lu, C. C. *J. Am. Chem. Soc.* **2013**, *135*, 13142.
(31) Zall, C. M.; Clouston, L. J.; Young, V. G., Jr.; Ding, K.; Kim, H. J.; Zherebetskyy, D.; Chen, Y.-S.; Bill, E.; Gagliardi, L.; Lu, C. C. *Inorg. Chem.* **2013**, *52*, 9216.
(32) Nippe, M.; Bill, E.; Berry, J. F. *Inorg. Chem.* **2011**, *50*, 7650.
(33) Nippe, M.; Victor, E.; Berry, J. F. *Eur. J. Inorg. Chem.* **2008**, 5569.
(34) Kuppuswamy, S.; Bezpalko, M. W.; Powers, T. M.; Turnbull, M. M.; Foxman, B. M.; Thomas, C. M. *Inorg. Chem.* **2012**, *51*, 8225.
(35) Kuppuswamy, S.; Powers, T. M.; Johnson, B. M.; Bezpalko, M. W.; Brozek, C. K.; Foxman, B. M.; Berben, L. A.; Thomas, C. M. *Inorg. Chem.* **2013**, *52*, 4802.

(36) Bailey, P. J.; Coxall, R. A.; Dick, C. M.; Fabre, S.; Henderson, L. C.; Herber, C.; Liddle, S. T.; Loroño-González, D.; Parkin, A.; Parsons, S. *Chem.—Eur. J.* **2003**, *9*, 4820.
(37) Wulf, R. *Acta Crystallogr.* **1990**, *A46*, 681.
(38) Toby, B. H.; Von Dreele, R. B. *J. Appl. Crystallogr.* **2013**, *46*, 544.
(39) O'Connor, C. J. *Prog. Inorg. Chem.* **1982**, *29*, 203.
(40) *CRC Handbook of Chemistry and Physics*, 59th ed.; Weast, R. C., Astle, M. J., Eds.; CRC Press: Boca Raton, FL, 1979.
(41) Kahn, O. *Molecular Magnetism*; VCH: Weinheim, Germany, 1993.
(42) Bill, E. *julX*, version 1.4.1; Germany, 2008.
(43) (a) Aquilante, F.; De Vico, L.; Ferré, N.; Ghigo, G.; Malmqvist, P.-Å.; Neogrády, P.; Pedersen, T. B.; Pitoňák, M.; Reiher, M.; Roos, B. O.; Serrano-Andrés, L.; Urban, M.; Veryazov, V.; Lindh, R. *J. Comput. Chem.* **2010**, *31*, 224. (b) Malmqvist, P. A.; Pierloot, K.; Shahi, A. R. M.; Cramer, C. J.; Gagliardi, L. *J. Chem. Phys.* **2008**, *128*, 204109.
(44) Roos, B. O.; Lindh, R.; Malmqvist, P.-Å.; Veryazov, V.; Widmark, P.-O. *J. Phys. Chem. A* **2004**, *108*, 2851.
(45) Roos, B. O.; Lindh, R.; Malmqvist, P.-Å.; Veryazov, V.; Widmark, P.-O. *J. Phys. Chem. A* **2005**, *109*, 6575.
(46) Douglas, M.; Kroll, N. M. *Ann. Phys.* **1974**, *82*, 89.
(47) Hess, B. A. *Phys. Rev. A* **1986**, *33*, 3742.
(48) Aquilante, F.; Pedersen, T. B.; Lindh, R. *J. Chem. Phys.* **2007**, *126*, 114107.
(49) Forsberg, N.; Malmqvist, P.-Å. *Chem. Phys. Lett.* **1997**, *274*, 196.
(50) Brynda, M.; Gagliardi, L.; Roos, B. O. *Chem. Phys. Lett.* **2009**, *471*, 1.
(51) Roos, B. O.; Borin, A. C.; Gagliardi, L. *Angew. Chem., Int. Ed.* **2007**, *46*, 1469.
(52) Noodleman, L. *J. Chem. Phys.* **1981**, *74*, 5737.
(53) Yamaguchi, K.; Takahara, Y.; Fueno, T. In *Applied Quantum Chemistry*; Smith, V. H., Jr., Schaefer, H. F., III, Morokuma, K., Eds.; Reidel: Boston, 1986; p 155.
(54) Frisch, M. J.; Trucks, G. W.; Schlegel, H. B.; Scuseria, G. E.; Robb, M. A.; Cheeseman, J. R.; Scalmani, G.; Barone, V.; Mennucci, B.; Petersson, G. A.; Nakatsuji, H.; Caricato, M.; Li, X.; Hratchian, H. P.; Izmaylov, A. F.; Bloino, J.; Zheng, G.; Sonnenberg, J. L.; Hada, M.; Ehara, M.; Toyota, K.; Fukuda, R.; Hasegawa, J.; Ishida, M.; Nakajima, T.; Honda, Y.; Kitao, O.; Nakai, H.; Vreven, T.; Montgomery, J. A., Jr.; Peralta, J. E.; Ogliaro, F.; Bearpark, M.; Heyd, J. J.; Brothers, E.; Kudin, K. N.; Staroverov, V. N.; Kobayashi, R.; Normand, J.; Raghavachari, K.; Rendell, A.; Burant, J. C.; Iyengar, S. S.; Tomasi, J.; Cossi, M.; Rega, N.; Millam, J. M.; Klene, M.; Knox, J. E.; Cross, J. B.; Bakken, V.; Adamo, C.; Jaramillo, J.; Gomperts, R.; Stratmann, R. E.; Yazyev, O.; Austin, A. J.; Cammi, R.; Pomelli, C.; Ochterski, J. W.; Martin, R. L.; Morokuma, K.; Zakrzewski, V. G.; Voth, G. A.; Salvador, P.; Dannenberg, J. J.; Dapprich, S.; Daniels, A. D.; Farkas, Ö.; Foresman, J. B.; Ortiz, J. V.; Cioslowski, J.; Fox, D. J. *Gaussian 09*, revision D.01; Gaussian, Inc.: Wallingford, CT, 2009.
(55) Ernzerhof, M.; Perdew, J. P. *J. Chem. Phys.* **1998**, *109*, 3313.
(56) Perdew, J. P.; Ernzerhof, M.; Burke, K. *J. Chem. Phys.* **1996**, *105*, 9982.
(57) Heyd, J.; Scuseria, G. E.; Ernzerhof, M. *J. Chem. Phys.* **2003**, *118*, 8207.
(58) Heyd, J.; Scuseria, G. E.; Ernzerhof, M. *J. Chem. Phys.* **2006**, *124*, 219906.
(59) Vydrov, O. A.; Scuseria, G. E. *J. Chem. Phys.* **2006**, *125*, 234109.
(60) Schäfer, A.; Horn, H.; Ahlrichs, R. *J. Chem. Phys.* **1992**, *97*, 2571.
(61) Schäfer, A.; Huber, C.; Ahlrichs, R. *J. Chem. Phys.* **1994**, *100*, 5829.
(62) Kim, M.; Kim, Y.-U.; Han, J. *Polyhedron* **2007**, *26*, 4003.
(63) Shin, B. K.; Kim, M.; Han, J. *Polyhedron* **2010**, *29*, 2560.
(64) Massoud, S. S.; Broussard, K. T.; Mautner, F. A.; Vicente, R.; Saha, M. K.; Bernal, I. *Inorg. Chim. Acta* **2008**, *361*, 123.
(65) *Multiple Bonds Between Metal Atoms*, 3rd ed.; Cotton, F. A., Murillo, C. A., Walton, R. A., Eds.; Springer: New York, 2005.
(66) Fohlmeister, L.; Liu, S.; Schulten, C.; Moubaraki, B.; Stasch, A.; Cashion, J. D.; Murray, K. S.; Gagliardi, L.; Jones, C. *Angew. Chem., Int. Ed.* **2012**, *51*, 8294.
(67) Freedman, D. E.; Han, T. H.; Prodi, A.; Müller, P.; Huang, Q.-Z.; Chen, Y.-S.; Webb, S. M.; Lee, Y. S.; McQueen, T. M.; Nocera, D. G. *J. Am. Chem. Soc.* **2010**, *132*, 16185.
(68) Nippe, M.; Berry, J. F. *J. Am. Chem. Soc.* **2007**, *129*, 12684.
(69) Lacy, D. C.; Gupta, R.; Stone, K. L.; Greaves, J.; Ziller, J. W.; Hendrich, M. P.; Borovik, A. S. *J. Am. Chem. Soc.* **2010**, *132*, 12188.
(70) Zhao, Q.; Betley, T. A. *Angew. Chem., Int. Ed.* **2011**, *50*, 709.
(71) Rivero, P.; Moreira, I. de P. R.; Illas, F.; Scuseria, G. E. *J. Chem. Phys.* **2008**, *129*, 184110.
(72) Valero, R.; Costa, R.; Moreira, I. de P. R.; Truhlar, D. G.; Illas, F. *J. Chem. Phys.* **2008**, *128*, 114103.